

Full length article

Plastic flow resistance of NiTiCu shape memory alloy-theory and experiments

S. Alkan¹, H. Sehitoglu*

Department of Mechanical Science and Engineering, University of Illinois at Urbana-Champaign, 1206 W. Green Street, Urbana, IL, 61801, USA

ARTICLE INFO

Article history:

Received 26 May 2018

Received in revised form

22 September 2018

Accepted 28 September 2018

Available online 3 October 2018

ABSTRACT

The NiTiCu alloys belong to a class of materials with excellent shape memory properties. The limitations in shape memory properties arise due to onset of slip at interfaces and also in austenite domains. As slip mediated plasticity is a source of irreversibility, it is imperative to understand the glide resistance of austenite which can be rather complex. In this paper, we develop a model to precisely derive the CRSS for slip substantiated with the uniaxial loading experiments on single crystals in a wide range of orientations employing Digital Image Correlation. We illustrate the core spreading of $\{011\}\langle 001 \rangle$ dislocations and evaluate the role of non-Schmid stress components which introduces profound anisotropy in CRSS levels. The model matches the experimental findings in single crystals with excellent agreement. The theory and experiments show significant crystal orientation dependence of plasticity which must be taken into account when designing with these alloys.

© 2018 Acta Materialia Inc. Published by Elsevier Ltd. All rights reserved.

1. Introduction

Research activities on a scientific understanding of shape memory alloys (SMAs) have been vigorously pursued [1,2] since the discovery of these alloys in the 1950s [3]. Many symposia (including the ICOMAT and ESOMAT series) have been devoted to shape memory alloys in the quest to understand their functional properties. All SMAs undergo stress-induced martensitic transformations that are recoverable [4], but in most cases the amount of recoverability falls short of the theoretical levels. The bedrock of these alloys still remains the near atomic NiTi which exhibits exceptional properties such as superelasticity and shape memory. Superelasticity represents transformation under stress cycling at constant temperature [5], while shape memory refers to transformation under temperature cycling at constant stress [6]. The previous foci on SMA research have been on experiments to measure the transformation strains and stresses, transformation hysteresis as well as continuum modelling of transformation and more recently atomistic studies [7,8]. These works are all foundational and too many to list. On the other hand, it is now clear that further studies are needed to understand the plasticity behavior as it

curtails the reversibility in this class of materials [9–15]. Characterization of plastic response in SMAs is a topic still at its infancy linked with the fact that the evolution of plastic deformation during transformation is highly localized and governed by complex stress states introduced at interfaces. These complex stress states are comprised of varying shear and normal character non-glide stress components as well as the glide shear stress acting along the activated slip system. In this study, we focus on the well-known NiTiCu alloys to understand the development of slip mediated plasticity in a homogenous material by utilizing single crystals. We undertook an experimental program of tension and compression stress states with different sample orientations. We chose cases where deformation develops without transformation to pinpoint the stress state effects. The work combines atomistic modelling with a continuum treatment of dislocations to develop a yield criterion for NiTiCu alloy.

The NiTiCu alloys exhibit a narrow hysteresis, low transformation stress levels and higher A_f (austenite finish) temperatures compared to the well-known NiTi [16,17]. These favorable attributes can be utilized in specific applications. Because they possess improved elastic compatibility at austenite-martensite interfaces compared to other SMAs [16,18], this can potentially impart favorable fatigue response. However, the NiTiCu is not as widely used as NiTi in industrial applications. Why? Apart from the limitations in bio-medical applications due to unfavorable corrosion/ion release, and the difficulty to coldwork to increase plastic flow

* Corresponding author.

E-mail address: huseyin@illinois.edu (H. Sehitoglu).¹ Current address: Department of Mechanical Engineering, Bogazici University, Bebek, Istanbul 34342, Turkey.

resistance, the NiTiCu exhibits smaller transformation strain near 6.6% [19–21] compared to NiTi and these strain magnitudes are smaller in comparison to theoretical predictions based on phenomenological theories [22]. This is possibly because dislocation-mediated slip can readily develop concurrently with stress-induced martensite especially at interfaces due to misfit strains. The localized slip effects can adversely impact shape memory functionality under cycling and degrade the fatigue impedance. These findings warrant a closer look at the intrinsic slip resistance of NiTiCu which is relatively unexplored. To interrogate the role of orientation and stress-state effect on dislocation-slip in isolation, it is imperative to conduct experiments at temperatures where slip occurs in the absence of transformation. Such experiments would permit the identification of the activated slip systems accurately and the determination of local resolved shear stress magnitudes. It is well known that CRSS (Critical Resolved Shear Stress) for slip may not correspond to a unique value and could exhibit strong orientation dependence, i.e. non-Schmid behavior. Based on this predicament, establishing a detailed understanding of slip resistance in this class of alloys and its precise determination is the topic of the current paper.

A primary reason for the non-unique CRSS levels in metals is that the dislocation core exhibits a non-planar structure and interplay with the applied stress components. The notion of a spread dislocation core is illustrated in Fig. 1 (a) and (b) which show two hypothetical cases with the same Burgers vector \mathbf{b} and distinct core structures: planar and non-planar respectively. As can be seen in Fig. 1 (a), for a planar dislocation, the lattice registry is confined to the slip plane. In this configuration, dislocation motion commences as the glide shear stress acting along the active slip system reaches a unique CRSS level (excluding glide resistance asymmetry dictated by the crystallographic symmetry arguments such as $\langle 111 \rangle \{112\}$ twin-antitwin slip asymmetry in bcc materials [23]). In contrast, for the non-planar cores as in Fig. 1 (b), the corresponding disregistry field extends over the conjugate planes which is the major reason for the interaction of core displacements

with the non-glide stress components as well as glide shear stress. In order to activate glide motion, the dislocation core tends to widen and increase its planarity under applied stress which decreases the crystal lattice resistance. To this end, as shown in Fig. 1 (c), the non-planar dislocation core requires in general a greater resolved shear stress to glide along the potential slip system compared to a planar one.

The major slip system in the NiTiCu alloys is $\{011\} \langle 100 \rangle$ where the dislocation core is expected to extend over multiple planes exhibiting a non-planar structure as in NiTi [14,15]. Inside the core region, the corresponding fractional dislocation arrangements are expected to interact with both glide and non-glide stress components leading the CRSS levels to exhibit strong anisotropy as a function of the loading state and single crystal orientation. In fact, even the sense of uniaxial loading whether it is tensile and compressive plays a key role and may cause significant differences in the CRSS levels for slip, denoted as tension-compression asymmetry [23]. Therefore to characterize plasticity in NiTiCu, there is a need to forward a generalized yield criterion that does overcome the limitations of the Schmid law. Following this motivation, in this work, uniaxial tension and compression experiments are conducted on single crystals of NiTiCu to precisely determine the resolved shear stress at the onset of slip. A wide range of single crystal orientations encompassing the stereographic triangle, i.e. $[001]$, $[012]$, $[011]$, $[112]$, $[123]$, $[122]$ and $[111]$, have been loaded under uniaxial tension and compression. This enabled us to draw a descriptive picture of the complex slip behavior of NiTiCu alloy. Notably, the results show that the variation of the resolved shear stress at the onset of yielding can vary by almost a factor of 2 which is significant and should be incorporated in any design efforts with NiTiCu.

On theoretical grounds, bcc based alloys exhibit non-planar core structure [23]. In the particular case of NiTi, it has been shown that the CRSS levels for the a $[001]$ (a: lattice parameter) dislocation to glide on a $\{110\}$ family plane may exhibit strong interplay with the applied stress components whether they are of

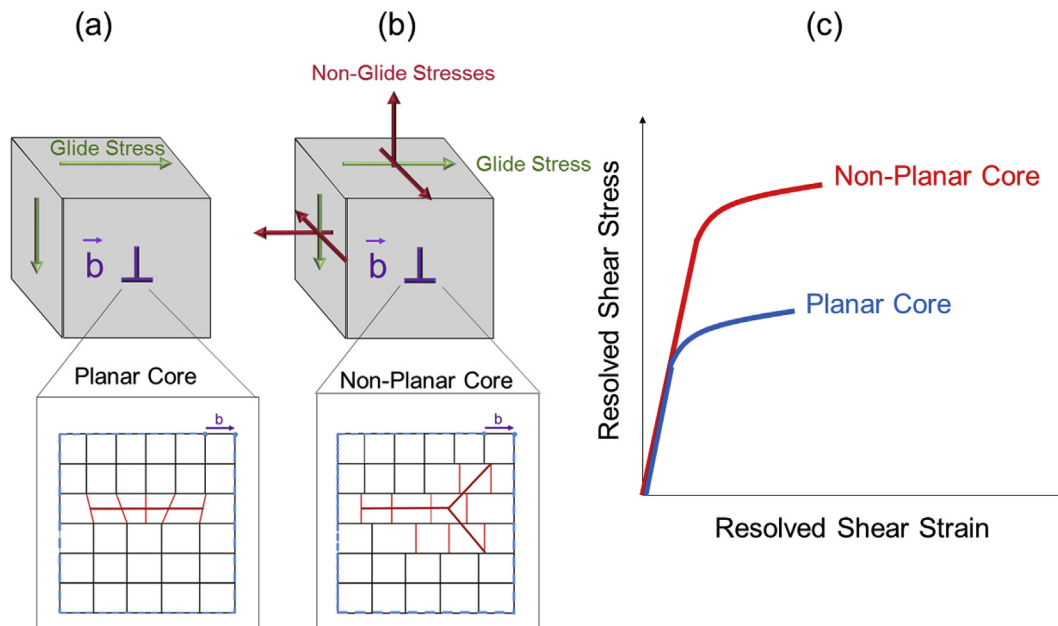


Fig. 1. (a) shows a planar dislocation structure with a Burgers vector \mathbf{b} in RH/FS convention. It is to be noted that only the glide shear along the slip system governs on the CRSS level for planar structure dislocations. (b) shows a non-planar core structure for the same Burgers vector \mathbf{b} . In this case, the core extends over multiple planes and the CRSS levels are affected by both glide and non-glide stresses. (c) shows the generic resolved shear stress vs resolved shear strain curves of planar and non-planar core structures along the active slip system.

glissile or non-glissile character [14,15]. On the other hand, a detailed theoretical framework which is capable of explaining the break-down of Schmid law at the onset of plastic flow in NiTiCu is yet to be established. Based on this motivation, in the present work, we aim to establish a formulation which can embrace the energy variation under applied stress in terms of both the dislocation field and atomistic scale displacements inside the dislocation core.

Meanwhile continuum theory of dislocations is employed to construct a long-range energy formulation, a modified Peierls-Nabarro expression which encompasses the lattice anisotropy involved, is derived to accurately determine the core extension at the atomistic scale. To accomplish this task, first-principles calculations, namely Density Functional Theory- DFT, are invoked to generate the Generalized Stacking Fault Energy-GSFE-profile along the $\{110\}\langle 001\rangle$ slip system [24]. The resolved shear stress acting along the active $\{110\}\langle 001\rangle$ glide system at the instant of vanishing convexity of the total energy expression enables us to determine the anisotropic CRSS levels for slip in NiTiCu. The resulting theoretical predictions are shown to be in excellent agreement with the experimental measurements suggesting the robustness of the underlying methodology.

Extending this novel theoretical framework fostered with both atomistic and continuum scale variables to the more general stress states paves the way to construct a generalized yield criterion for NiTiCu. This modified criterion helps us to incorporate the contribution of both glide and non-glide stress components liberating the theoretical predictions from the limitations of Schmid law which is solely based on the presence of a hypothetical unique critical glide shear stress [25]. This modified yield criterion serves as a profound improvement over the earlier crystal plasticity efforts [26,27] based on Schmid law as the anisotropic slip onset behavior can be captured with higher accuracy. In parallel with these efforts, an anisotropic yield parameter η is defined as a measure to directly compare the extent of anisotropy in yield surfaces on numerical grounds.

Considering that the transformation temperatures and the glide resistance are of paramount importance in optimizing the functional performance of NiTi based shape memory alloys, addition of a ternary element stands out as a beneficial method for achieving this goal [20]. A rich literature has also evolved showing that ternary alloying element additions such as Au, Pd, Pt introduce an increase in the M_s temperature [28–32]. In contrast, the ternary elements of Co, Fe, Mn, Al, Cr and V are known to lower M_s [31,33]. For Cu compositions lower than 20 at.%, the two stage transformation in NiTiCu lead to different trends in response to Cu alloying. Meanwhile M_s temperature for B2 to B19 transformation is promoted with Cu addition, an opposite trend is observed for B19 to B19' [34,35]. In both cases, M_s temperature can be predicted employing Clausius-Clapeyron slope based on transformation latent heat measurements [36,37]. On the other hand, the effects of ternary alloying elements on the slip resistance has yet to be established for NiTiCu based shape memory alloys. In this work, we interrogate on the addition of Cu effect with experiments and

theory encompassing a wide range of sample orientations that is missing in the literature.

Associated with plasticity, there is a redistribution of internal stresses which can produce residual austenite and residual martensite as well as affecting the variants that are contributing to the shape memory process [38]. There is also an important discussion on the role of plasticity in assisting heterogeneous transformation [39]. Consequently, the present work aims to instigate further studies on characterization of dislocation mobility in SMAs which plays a prominent role in the functional properties of this class of materials. The theory developed is checked against new experimental results for 14 single crystal orientations under uniaxial tension and compression stress states. Taken as a whole, the paper represents a comprehensive collection of new experimental results and theoretical predictions.

2. Experimental methods

The material was originally cast with atomic percentages of 49.5 at.% Ti, 9.1 at.% Cu and 41.4 at.% Ni. Single crystals were grown in an inert environment by Bridgman technique. The single crystals were solutionized for 1193 K for 24 h followed by water quench. This heat treatment results in transformation temperatures of $A_s = 273$ K, $A_f = 304$ K, $M_s = 294$ K and $M_f = 262$ K which are determined by conducting heating-cooling cycles at a rate of 10 K/min by Differential Scanning Calorimetry (DSC). At this stage, it is to be emphasized that in NiTiCu, a two-stage transformation path is observed such that (i) B2 to B19 and (ii) B19 to B19'. On the other hand, we will not demarcate the successive transformation stages as the corresponding peaks are inseparable in DSC analyses for the solutionized sample [40–42] and our main focus is on the dislocation mediated plasticity in austenite phase of B2 structure. Following the heat treatment, the crystallographic orientations of samples were determined with Electron Backscatter Diffraction (EBSD) by JEOL 7000 F Scanning Electron Microscope (SEM). We have selected several crystal orientations and conducted multiple experiments to ensure the repeatability of the results. The uniaxial loading orientations focused in this study are [012] in tension and [123], [122], [112], [011], [111], [001] in tension and compression. Therefore, a detailed coverage of the stereographic triangle is obtained which allows for a thorough interrogation of the contribution of glide and non-glide resolved stresses on the anisotropic slip behavior in NiTiCu.

The crystallographic orientations of the samples are provided in Table 1 employing the orthonormal sample frame $\mathbf{E}_1 - \mathbf{E}_2 - \mathbf{E}_3$ demonstrated in Fig. 2. The sample orientations are described such that \mathbf{E}_2 is parallel to the unit normal of the plane along which the uniaxial loading acts and \mathbf{E}_3 is parallel to the normal of the surface on which the axial strain field is generated by employing Digital Image Correlation (DIC) technique. The effect of the applied stress state is calculated employing the orthonormal dislocation frame $\mathbf{e}_1 - \mathbf{e}_2 - \mathbf{e}_3$ in which \mathbf{e}_2 and \mathbf{e}_3 are parallel to the slip plane normal and glide direction vectors.

Table 1

Shows the crystallographic vector triads which are parallel to the $\mathbf{E}_1 - \mathbf{E}_2 - \mathbf{E}_3$ sample frame base vectors for each sample orientation. It is to be noted that the triad $\mathbf{E}_1 - \mathbf{E}_2 - \mathbf{E}_3$ is same for tension and compression samples of a specific loading orientation.

[011] Sample	[111] Sample	[123] Sample
$[1\ 5\ \bar{5}] - [0\ 1\ 1] - [10\ \bar{1}\ 1]$	$[3\ 4\ \bar{7}] - [1\ 1\ 1] - [11\ \bar{10}\ \bar{1}]$	$[0\ 3\ \bar{2}] - [1\ 2\ 3] - [5\ 2\ \bar{3}]$
[122] Sample	[112] Sample	[012] Sample
$[0\ 1\ \bar{1}] - [1\ 2\ 2] - [4\ \bar{1}\ \bar{1}]$	$[1\ \bar{1}\ 0] - [1\ 1\ 2] - [\bar{1}\ \bar{1}\ 1]$	$[4\ 2\ \bar{1}] - [0\ 1\ 2] - [5\ \bar{8}\ 4]$

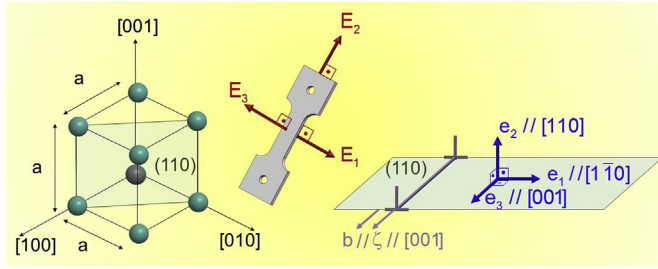


Fig. 2. shows the cubic crystal frame in B2 ordered NiTiCu, the orthonormal sample frame $E_1 - E_2 - E_3$ and the local dislocation frame $e_1 - e_2 - e_3$. Note that b corresponds to $a[001]$ Burgers vector and ζ is the unit dislocation line parallel to the Burgers vector.

The uniaxial tension and compression experiments are conducted employing an MTS servo-hydraulic load frame with an average strain rate of $5 \times 10^{-5} \text{ s}^{-1}$. The experiments are conducted at 393 K ensuring the B2 ordered austenitic structure. Tensile dog bone samples employed are of 8 mm gage length with 1.5 mm thickness meanwhile compression sample dimensions are of 8 mm \times 4 mm \times 4 mm. The experimented samples are cut by Electro Discharge Machining (EDM). The in-situ full-scale deformation field is generated by DIC technique employing a CCD camera which tracks a special pattern deposited on mirror polished sample surfaces with a resolution of 3microns/pixel. The resulting displacement and strain fields are utilized to pinpoint the onset of slip and to measure the CRSS levels acting on the active slip systems which are determined by employing two-surface trace analyses under both optical and Scanning Electron Microscopy (SEM) imaging. It is to be emphasized that such a detailed local analysis is necessary to determine the accurate CRSS levels which exhibit a substantial improvement over the conventional yield-offset methods based on macroscale behavior.

Detailed EBSD analyses are conducted on each sample experimented in order to verify that the anisotropy of CRSS levels along $\{110\}\langle 100\rangle$ slip system stems from the slip mediated plasticity in fully austenitic regime but not from the lattice invariant shear accompanying martensitic transformations from B2 to B19 and B19 to B19', or detwinning. As martensitic transformation stress and strain levels may also exhibit deviations from Schmid law [43,44], this post-deformation analysis is of substantial importance to ensure that the reported break-down of Schmid law is imparted solely by slip-mediated plasticity.

In this study, two geometric frameworks will be employed to distinguish the crystallographic orientation of the samples,

governing on the applied stress state and the loading sense, i.e. tensile or compressive character. In order to accomplish this task, two angles will be introduced, i.e. χ and θ . The χ angle convention for $\{110\}\langle 100\rangle$ slip system distinguishes the sample orientation and loading sense effects by measuring the angle between the maximum resolved shear stress plane (MRSSP), i.e. the plane which bears the highest resolved shear stress along the active $\{110\}\langle 100\rangle$ system, and the reference $\{110\}$ plane which is commonly chosen as the plane bearing the highest resolved shear stress among the possible $\{110\}$ planes. It is to be noted that no restriction on the MRSSP is imposed such that it can be any plane with either rational or irrational character. The corresponding geometric convention is illustrated in Fig. 3(a). The symmetry of B2 structure within the $\{110\}\langle 100\rangle$ slip zone imposes a bound on the χ angle such that it varies from 0° to 45° .

The second convention, which is a novel improvement introduced in this study, employs the pole projection angle of θ formed between the $\langle 100\rangle$ normal direction and the connecting line drawn from the projection of a generic $\langle hkl\rangle$ sample orientation and the tip of the unit $\langle 100\rangle$ vector. This is illustrated in Fig. 3(b). On mathematical grounds, the angle θ for $\langle hkl\rangle$ orientation can be expressed as (satisfying $\sqrt{h^2 + k^2 + l^2} = 1$)

$$\theta = \tan^{-1} \left((\sqrt{2} + 1) \sqrt{\frac{h^2 + k^2}{(1 + l)^2}} \right) \quad (1)$$

In the expression given in Eq. (1), the multiplying factor $(\sqrt{2} + 1)$ is derived based on normalization of the projected $[001]$ - $[011]$ distance. This novel pole projection θ angle convention results in a smooth and bijective mapping such that the tuple (χ, θ) can uniquely distinguish the sample orientation considering the cubic space group.

3. Theoretical modelling of anisotropic slip resistance in NiTiCu

Deviations from Schmid law are well known in bcc and ordered cubic alloys [15,45–47]. Experiments and modelling efforts have mainly documented the non-Schmid behavior in pure transition metals such as Mo, Nb, Ta and others (for a review see Ref. [23]). Recently, current authors have demonstrated the non-Schmid response in B2 (NiTi) and DO₃ ordered (Fe₃Al) alloys that exhibit shape memory behavior [14,15,47]. As a first step towards modelling the anisotropic CRSS levels in NiTiCu, we conducted DFT calculations via employing Vienna Ab-Initio Simulation Package (VASP) to calculate the B2 ordered NiTiCu lattice parameter, a , and generate the GSFE profile along $\{110\}\langle 100\rangle$. In DFT calculations,

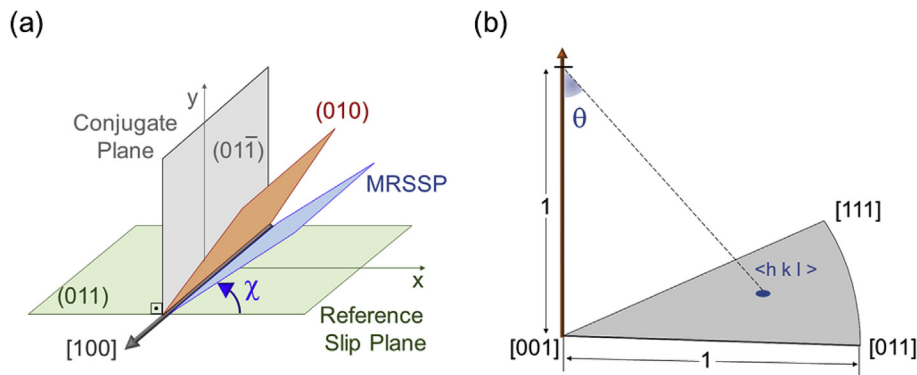


Fig. 3. (a) The geometry of the MRSSP χ angle convention illustrated for an exemplary configuration in which $(011)[100]$ slip system is active. (b) The geometry of pole projection θ angle is illustrated for an arbitrary crystallographic loading direction $\langle hkl\rangle$ on the $[001]$ - $[011]$ - $[111]$ stereographic triangle.

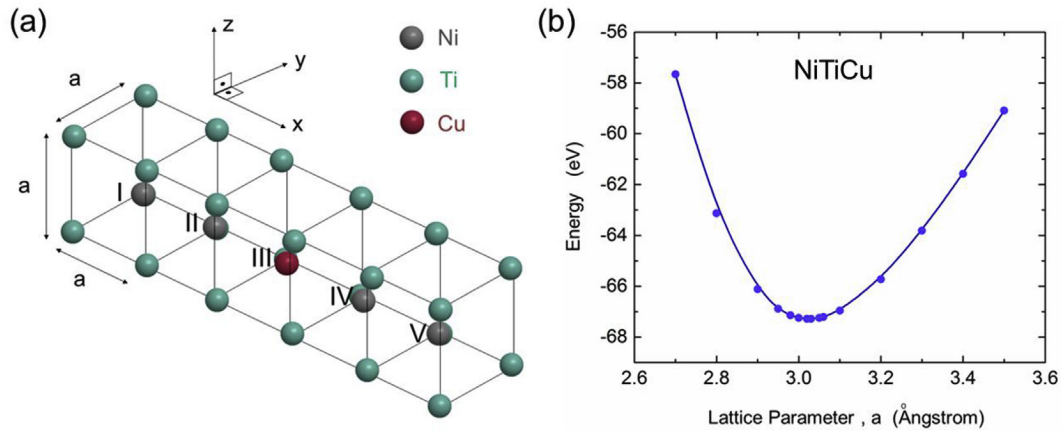


Fig. 4. (a) shows a unit block of $5 \times 1 \times 1$ B2 ordered $\text{Ni}_4\text{Ti}_5\text{Cu}_1$. To construct the $5 \times 3 \times 3$ supercell, on the x-y plane, the Cu atoms are located at the set of body centered sites of {III, I, V}, {II, IV, II} and {I, III, V} for each layer along z direction. The rest of the body centered sites are occupied by Ni atoms and the corner sites are of Ti atoms. (b) shows the variation of structural energy with the lattice parameter a . The resulting minimum of the structural energy corresponds to 3.020 Angstroms which is in excellent agreement with the experimental value of 3.015 Angstroms [10].

we utilized projector augment wave (PAW) method with generalized gradient approximation (GGA) [48,49]. To determine the lattice constant of $\text{Ni}_4\text{Ti}_5\text{Cu}_1$ nominal composition, we delineated a 90 atom supercell with a size of $5 \times 3 \times 3$. The positions of the atoms in B2 structure are shown in Fig. 4 (a) as of $5 \times 1 \times 1$ which is determined based on an iterative search effort to minimize the total structural energy. The body centered positions are enumerated in Roman numerals, {I, II, III, IV, V}; and they are the possible occupation sites of Cu atoms. For each layer along z direction, the atoms of Cu occupy the following set of lattice sites: {III, I, V}, {II, IV, II} and {I, III, V} where the rest of the body centered sites are occupied by Ni atoms with Ti atoms located at the corner sites.

The resulting structural energy versus lattice parameter is plotted in Fig. 4 (b). The minimum of the structural energy corresponds to the equilibrium lattice parameter which is equal to

3.020 Angstroms. At this stage, it is to be noted that this theoretical lattice parameter exhibits an excellent agreement with the X-ray diffraction and electron microscopy measurements of Bricknell et al. [50] which corresponds to 3.015 Angstroms for the same nominal composition. The GSFE profile, namely γ curve, is generated by employing the same supercell of lattice parameter calculations and plotted in Fig. 5. The atomic slip disregistry, u , across the active glide plane of (011) varies between 0 to $|a\langle 100 \rangle|$ and is normalized with the lattice parameter, a , which is also equal to the Burgers vector magnitude $b = |a\langle 100 \rangle|$. The crystal configurations at $u = 0$ and $u = a/2$ [100] are illustrated in Fig. 5 (a) and (b). As a first observation, the γ curve along $\{110\} \langle 100 \rangle$ slip system in NiTiCu exhibits a single peak which suggests that no stable stacking fault formation is allowed along this system similar to B2 ordered equi-atomic NiTi [14]. Secondly, the unstable

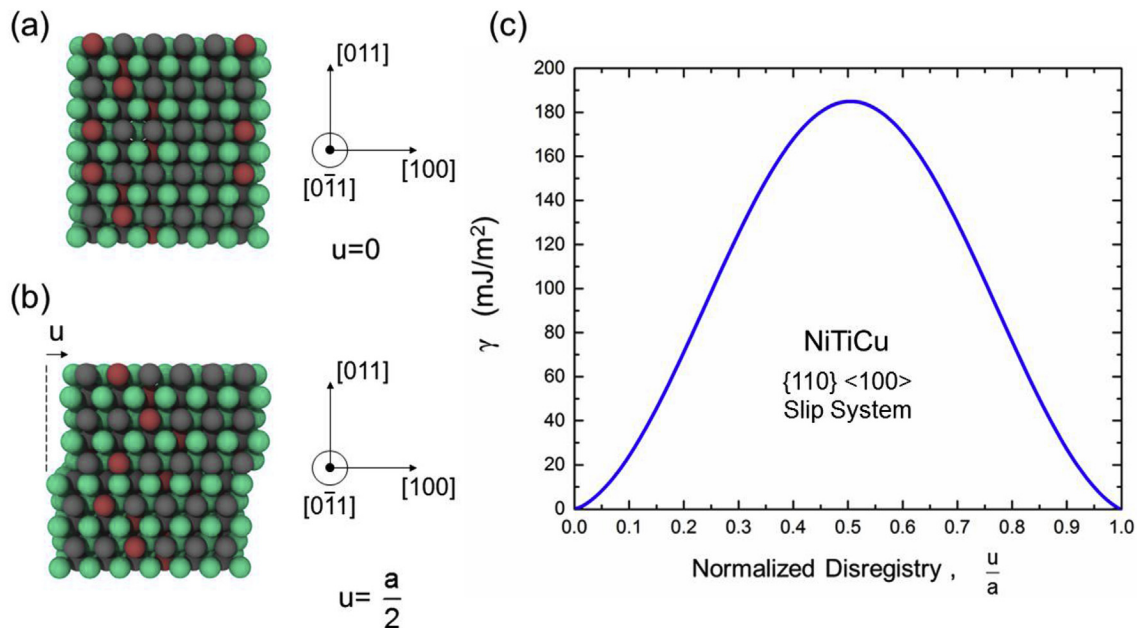


Fig. 5. (a) shows the pristine crystal configuration, i.e $u = 0$. (b) shows the crystal configuration corresponding to a disregistry of $u = a/2$ [100] on (011) plane. (c) The GSFE, namely γ , profile for $\{110\} \langle 100 \rangle$ glide system is plotted. It is to be noted that the local maximum along the γ curve which corresponds to the unstable stacking fault energy, γ^{us} , is equal to 185 mJ/m².

stacking fault energy, γ^{us} , which corresponds to the local maximum along the γ curve and plays a key role in slip modelling efforts is determined to be 185 mJ/m².

Earlier simulation results on B2 ordered NiTi in which the plastic deformation is accommodated by slip along {110} <100> suggest that the relaxed screw dislocation core in both externally stress-free configuration and under applied stress extends over multiple planes which is typical of bcc derivative structured metals and alloys [14]. Considering the quadrupole symmetric structure of a <100> screw dislocations within the absence of external stress in B2 alloys, we modelled the distribution of disregistry displacements along the active and conjugate {110} family planes which intersect each other at 90° within the <100> slip zone as shown in Fig. 2 (a). Based on the earlier literature evolved around the description of defect structures via continuum field theories [51–53], we employed the following two disregistry functions $f_1(x)$ and $f_2(y)$ as follows:

$$f_1(x) = \sum_{i=1}^2 \frac{\alpha_i b}{\pi} \left[\tan^{-1} \left(\frac{x-x_i}{c_i \xi_1} \right) + (c_i - 1) \xi_1 \frac{x-x_i}{(x-x_i)^2 + (c_i \xi_1)^2} \right] + \frac{b}{2} \quad (2)$$

$$f_2(y) = \sum_{i=3}^4 \frac{\alpha_i b}{\pi} \left[\tan^{-1} \left(\frac{y-y_{i-2}}{c_i \xi_2} \right) + (c_i - 1) \xi_2 \frac{y-y_{i-2}}{(y-y_{i-2})^2 + (c_i \xi_2)^2} \right] + \frac{b}{2} \quad (3)$$

with the constraints of:

$$0 < |\alpha_i| \leq 1 \quad (4.a)$$

$$\alpha_1 + \alpha_2 = 1 \quad (4.b)$$

$$\alpha_3 + \alpha_4 = 0 \quad (4.c)$$

In the expressions Eqs. (2) and (3), $\alpha_i b$ ($i = 1, 2, 3, 4$) correspond to the resultant Burgers vectors of fractional dislocations, x_i and y_i ($i = 1, 2$) are the centers of the resultant fractional dislocation positions; c_i ($i = 1, 2, 3, 4$), ξ_1 and ξ_2 are the free parameters governing on the width of the core structure. Considering the two set of equations, i.e. Eqs. (2) and (3), there are fourteen unknown parameters to determine the core disregistry functions $f_1(x)$ and $f_2(y)$, i.e. $\{\alpha_1, \alpha_2, \alpha_3, \alpha_4, c_1, c_2, c_3, c_4, \xi_1, \xi_2, x_1, x_2, y_1, y_2\}$. The disregistry functions differ from the original treatment of Peierls-Nabarro [54,55] in multiple aspects: (i) they capture the contribution of both screw and edge character slip displacements, (ii) they are anisotropic as the free parameters are solved incorporating the atomistically-informed GSFE profile and the particular elastic shear modulus along the {110} <100> slip system, (iii) the non-planar spreading of the dislocation core along the conjugate {110} plane is embedded in the formulation.

To solve for the free parameters, we need fourteen equations the two of which are expressed in Eq. (4b) and Eq. (4c). To construct the remaining twelve equations, we introduce the dislocation density functions $\rho_1(x)$ and $\rho_2(y)$ which are defined as spatial derivatives of the disregistry functions $f_1(x)$ and $f_2(y)$ respectively as follows:

$$\rho_1(x) = \frac{\partial f_1}{\partial x} \quad (5)$$

$$\rho_2(y) = \frac{\partial f_2}{\partial y} \quad (6)$$

As the dislocations are localized character slip defects, the following boundary conditions are to be satisfied which imposes attenuation of the disregistry fields at far-field:

$$\lim_{x \rightarrow \infty} \rho_1(x) = 0 \quad (7)$$

$$\lim_{x \rightarrow -\infty} \rho_1(x) = 0 \quad (8)$$

$$\lim_{y \rightarrow \infty} \rho_2(y) = 0 \quad (9)$$

$$\lim_{y \rightarrow -\infty} \rho_2(y) = 0 \quad (10)$$

The remaining eight equations are derived from the energy minimization criterion which dictates the construction of a total energy functional $E^{total} : E^{total}(\alpha_1, \alpha_2, \alpha_3, \alpha_4, c_1, c_2, c_3, c_4, \xi_1, \xi_2, x_1, x_2, y_1, y_2)$ composed of both short-range and long-range energy terms. Among the long range energy terms, the self, E^{self} , and interaction, E^{inter} , energies of the core fractionals can be expressed as [56]:

$$E^{self} = \frac{K}{\pi} \int_{-\infty}^{\infty} \int_{-\infty}^{\infty} \rho_1(t) \rho_1(x) \ln(t-x) dt dx + \frac{K}{\pi} \int_{-\infty}^{\infty} \int_{-\infty}^{\infty} \rho_2(t) \rho_2(y) \ln(t-y) dt dy \quad (11)$$

$$E^{inter} = -\frac{K}{2\pi} \int_{-\infty}^{\infty} \int_{-\infty}^{\infty} \rho_1(x) \rho_2(y) \ln \left| \frac{R}{x^2 + xy + y^2} \right| dx dy \quad (12)$$

where t is a dummy variable and R is outer radius which is taken as 500 nm. K is an anisotropic parameter equal to elastic modulus C_{44} (in Voigt notation) along <100>, i.e. equal to $C_{44} = 47$ GPa, where C_{11} and C_{12} are set equal to 193 GPa and 175 GPa based on the first principles calculations for a similar chemical composition, Ni_{43.75}Ti₅₀Cu_{6.25} (at.%), in the earlier literature [57]. The modulus along the glide sense in energy calculations manifests the anisotropy of the formulation utilized in the present work. Furthermore, the short-range energy term $E^{stacking}$ corresponding to the generalized stacking faults formed by the fractionals centered at x_1, x_2, y_1 and y_2 as:

$$E^{stacking} = \int_{-\infty}^{\infty} \gamma(f_1(x)) dx + \int_{-\infty}^{\infty} \gamma(f_2(y)) dy \quad (13)$$

The total energy functional E^{total} is expressed as the sum of the individual energy terms of E^{self} , E^{inter} and $E^{stacking}$ in addition to the applied work, W :

$$E^{total} = E^{self} + E^{inter} + E^{stacking} - W \quad (14)$$

where W is defined as:

$$W = \int_{-\infty}^{\infty} \delta_{i3} \Sigma_{ij} n_j f_1(x) dx + \int_{-\infty}^{\infty} \delta_{i2} \Sigma_{ij} n_j f_2(y) dy \quad (15)$$

The minimum energy configuration under an applied stress tensor Σ dictates the following mathematical expressions:

$$\frac{\partial E^{total}}{\partial c_i} = 0 \quad (i = 1, 2, 3, 4) \quad (16)$$

$$\frac{\partial E^{total}}{\partial \xi_1} = 0 \quad (17)$$

$$\frac{\partial E^{total}}{\partial \xi_2} = 0 \quad (18)$$

$$\frac{\partial E^{total}}{\partial x_1} = 0 \quad (19)$$

$$\frac{\partial E^{total}}{\partial y_1} = 0 \quad (20)$$

Based on the fourteen equations, i.e. Eq. (4b), (4c), (7), (8), (9), (10), (16), (17), (18), (19) and (20); the set of fourteen unknowns $\{c_1, c_2, c_3, c_4, \xi_1, \xi_2, \alpha_1, \alpha_2, \alpha_3, \alpha_4, x_1, x_2, y_1, y_2\}$ are solved.

3. Results

3.1. Experimental results

The stress vs strain curves under uniaxial compression are plotted in Fig. 6 (a) for [011], [001], [123], [111], [122], [112] and [012] samples. The corresponding slip traces resulting from the localization of the axial strain is shown for each sample orientation in Fig. 6 (b). Among these, [001] compression sample exhibits twinning prior to slip induced plasticity; therefore, the CRSS for slip in this particular orientation will not be further expounded as our main focus in this work is on the slip initiation in pristine crystals. The active glide systems of the remaining six orientations are tabulated in Table 2 along with the CRSS values in Table 3. As can be seen in Table 3, the CRSS values under compression varies as a function of single crystal orientation exhibiting non-Schmid behavior.

The orientations of [001], [111], [011], [112], [122] and [123] are also experimented under uniaxial tension and the resulting stress-strain curves are plotted in Fig. 7 (a). The corresponding uniaxial

Table 2

The activated slip planes of the experimented samples under uniaxial tension and compression are tabulated. The slip plane normal is parallel to the base vector of e_2 whereas e_3 vector is set to be parallel to the slip direction.

Crystal Orientation	Compression	Tension
[122]	(110) [00 $\bar{1}$]	(110) [001]
[112]	(011) [$\bar{1}00$]	(011) [100]
[123]	(110) [00 $\bar{1}$]	(110) [001]
[012]	(110) [00 $\bar{1}$]	–
[011]	(101) [0 $\bar{1}0$]	(101) [010]
[111]	(011) [$\bar{1}00$]	(011) [100]

Table 3

shows the CRSS values as a function of crystal orientation measured under uniaxial compression and tension.

Crystal Orientation	Compression (MPa)	Tension (MPa)
[122]	114.4	162
[112]	130.7	175.4
[123]	200.1	117.5
[012]	205.8	–
[011]	109.6	148
[111]	163.2	121.2

strain field generated by DIC at the onset of plastic slip are also shown in Fig. 7 (b). The CRSS levels and the active slip systems are tabulated in Tables 2 and 3. Among this set of samples, [001] tension sample exhibits brittle fracture and as shown in Fig. 7 (b), there is no clear slip trace detected prior to failure. To this end, this sample is excluded from Tables 1 and 2. The resulting CRSS values demonstrate the break-down of Schmid law.

Fig. 8 (a) and (b) show the CRSS values plotted against both MRSSP χ angle and the novel convention of pole projection θ angle, respectively. As can be seen, the highest CRSS level along the active {110} <100> systems is measured for [012] orientation under compression with a level of 205.8 MPa. On the other hand, the minimum level of CRSS correspond to the [011] sample with 109.6 MPa. Among the available data set, the largest tension-compression asymmetry is measured for [123] sample orientation which is 82.6 MPa.

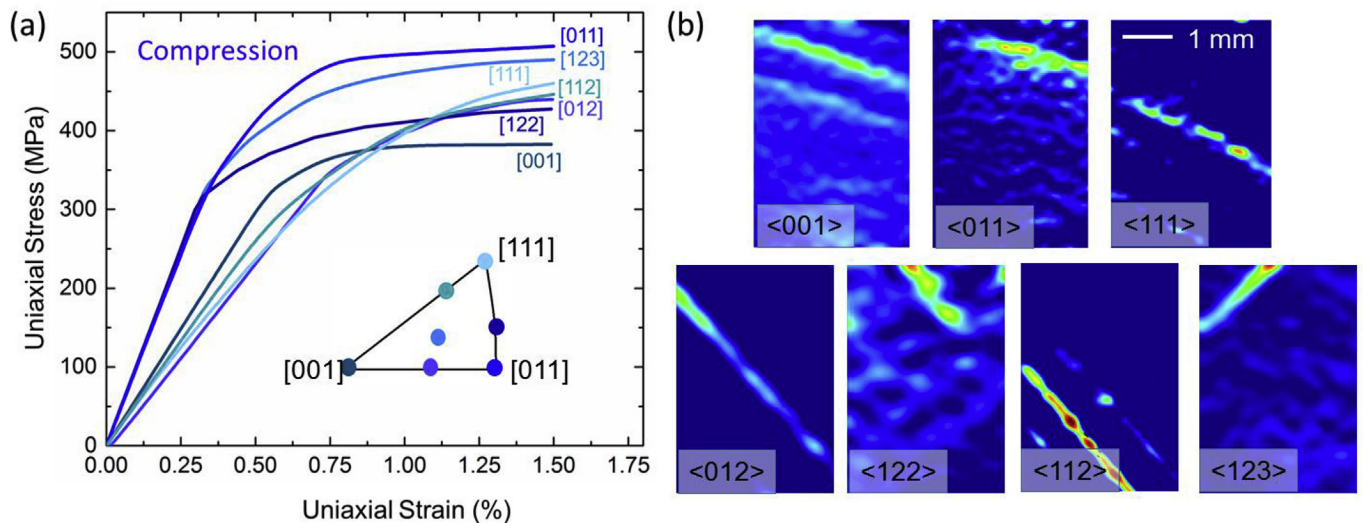


Fig. 6. (a) Stress vs strain graphs for [001], [122], [012], [112], [111], [123], [011] uniaxial compression samples are plotted at a strain rate of $5 \times 10^{-5} \text{ s}^{-1}$. (b) shows the localization of uniaxial strain field at the onset of slip along the tabulated slip systems in Table 1 and the corresponding CRSS levels Table 2 below.

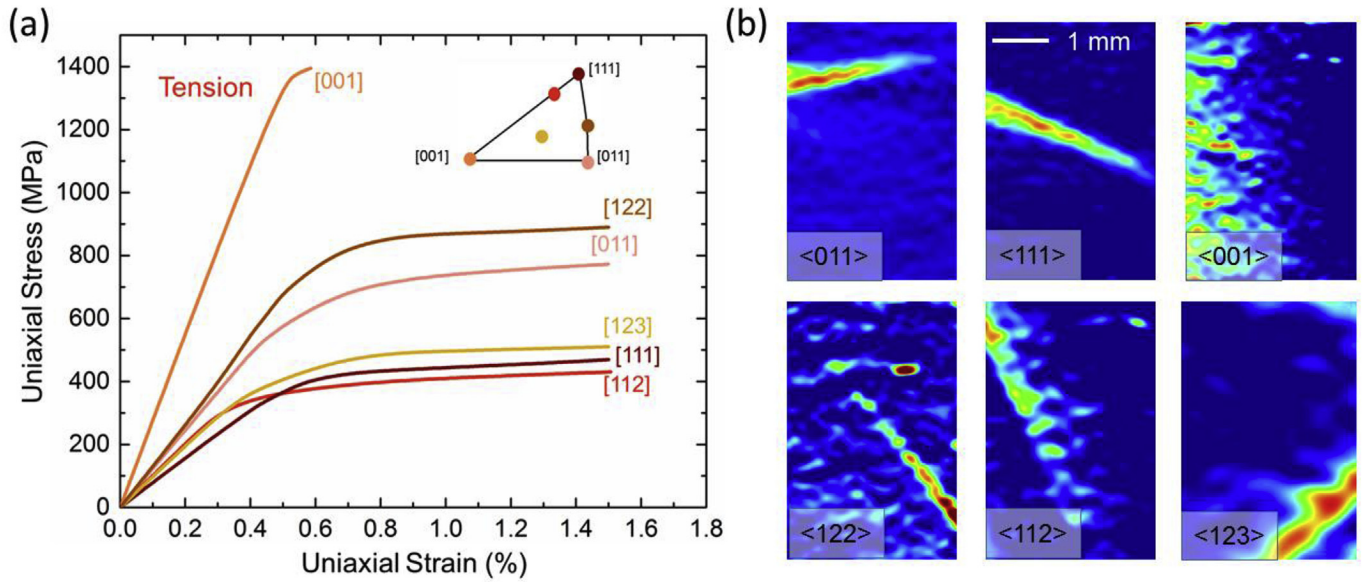


Fig. 7. (a) Stress vs strain graphs for [001], [122], [112], [111], [123], [011] uniaxial tension samples are plotted at a strain rate of $5 \times 10^{-5} \text{ s}^{-1}$. (b) shows the localization of uniaxial strain field at the onset of slip along the tabulated slip systems in Table 1 and the corresponding CRSS levels Table 2 below.

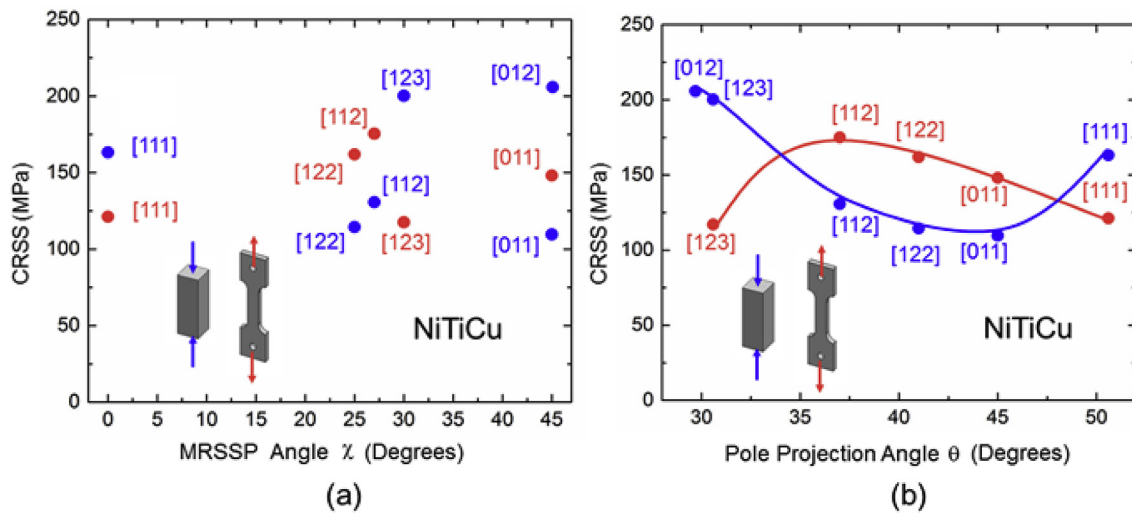


Fig. 8. (a): The variation of CRSS of {110} <100> slip system under tension and compression with χ angle is plotted suggesting the break-down of Schmid law. (b) The variation of CRSS of {110} <100> slip system under tension and compression with θ angle is plotted suggesting strong deviations from Schmid law which presumes a constant CRSS level irrespective of θ .

Table 4

Applied stress tensors in $\mathbf{e}_1 - \mathbf{e}_2 - \mathbf{e}_3$ frame at the onset of slip for each sample crystallographic orientation are shown for compression. The superscript “C” stands for compression. The units are given in MPa and the CRSS levels are shown in bold face.

$\Sigma^{011C} = \begin{bmatrix} -77.47 & -77.47 & 108.46 \\ -77.25 & -77.47 & 108.46 \\ 108.46 & 108.46 & -154.95 \end{bmatrix}$	$\Sigma^{111C} = \begin{bmatrix} 0 & 0 & 0 \\ 0 & -231.95 & 162.71 \\ 0 & 162.71 & -114.24 \end{bmatrix}$	$\Sigma^{123C} = \begin{bmatrix} -13.20 & -44.01 & 66.01 \\ -44.01 & -140.83 & 198.04 \\ 66.01 & 198.04 & -286.06 \end{bmatrix}$
$\Sigma^{122C} = \begin{bmatrix} -12.13 & -38.83 & 36.40 \\ -38.83 & -121.35 & 114.07 \\ 36.40 & 114.07 & -109.21 \end{bmatrix}$	$\Sigma^{112C} = \begin{bmatrix} -29.56 & -92.40 & 40.65 \\ -92.40 & -277.20 & 129.36 \\ 40.65 & 129.36 & -62.83 \end{bmatrix}$	$\Sigma^{012C} = \begin{bmatrix} -72.72 & -72.72 & 203.61 \\ -72.72 & -72.72 & 203.61 \\ 203.61 & 203.61 & -581.76 \end{bmatrix}$

The stress tensor acting on each sample orientation $\langle hkl \rangle$ in cubic frame is denoted as Σ^{hkl} and its components are tabulated in Tables 4 and 5 in dislocation coordinate frame $\mathbf{e}_1 - \mathbf{e}_2 - \mathbf{e}_3$ (for all samples except [001] compression and tension samples in which

deformation twinning and cleavage mechanisms are activated before slip). The CRSS levels plotted in Fig. 8 exhibit strong anisotropy linked with the stress components acting in the active and conjugate slip planes for each sample. As the GSFE curve along

Table 5

Applied stress tensors in $\mathbf{e}_1 - \mathbf{e}_2 - \mathbf{e}_3$ frame at the onset of slip for each sample crystallographic orientation are shown for tension. The superscript “T” stands for tension. The units are given in MPa and the CRSS levels are shown in bold face.

$\Sigma^{011T} = \begin{bmatrix} 104.63 & -104.63 & -148 \\ -104.63 & 104.63 & 148 \\ -148 & 148 & 209.27 \end{bmatrix}$	$\Sigma^{111T} = \begin{bmatrix} 0 & 0 & 0 \\ 0 & 171.40 & 121.19 \\ 0 & 121.19 & 85.69 \end{bmatrix}$	$\Sigma^{123T} = \begin{bmatrix} 9.22 & -27.68 & -39.16 \\ -27.68 & 83.08 & 117.51 \\ -39.16 & 117.51 & 166.19 \end{bmatrix}$
$\Sigma^{122T} = \begin{bmatrix} 19.09 & -57.28 & -53.98 \\ -57.28 & 171.83 & 162 \\ -53.98 & 162 & 152.72 \end{bmatrix}$	$\Sigma^{112T} = \begin{bmatrix} 41.32 & -124.02 & -58.49 \\ -124.02 & 372.07 & 175.42 \\ -58.49 & 175.42 & 82.70 \end{bmatrix}$	$\Sigma^{012T} = \begin{bmatrix} 37.48 & -37.48 & -106 \\ -37.48 & 37.48 & 106 \\ -106 & 106 & 299.85 \end{bmatrix}$

{110} <100> slip system is of symmetric shape, the resulting asymmetry in CRSS values under tension and compression is associated with the interplay between the non-planar dislocation core and the applied stress tensor. It is to be noted that the anisotropy in CRSS levels is substantial and extends up to 100 MPa among the sample orientations focused (i.e. max. CRSS = 205.8 MPa and min. CRSS = 106 MPa).

3.2. Theoretical results

To establish a theoretical frame to unveil the interplay between the core registry and the applied loading, as a first step, we determined the $\rho_1(x)$ and $\rho_2(y)$ functions within the externally stress-free configuration as demonstrated in Fig. 9 (a) along with the corresponding parameters tabulated in Table 6. The symmetric distributions of $\rho_1(x)$ and $\rho_2(y)$ have a maximum of 0.36 b and 0.20 b respectively. As a following step, we focused on a scenario in which pure glide shear stress, Σ_{23} , acts on the {110}<100> system. This allows us to distinguish the contribution of individual non-glide stress components in the following steps. The resulting core configuration is illustrated in Fig. 9 (b) via the functions of $\rho_1(x)$ and $\rho_2(y)$ plotted. The corresponding parameters are also included in Table 6.

The most distinguishing feature of the screw dislocation core structure under Σ_{23} compared to the stress-free configuration is

Table 6

The tabulated free parameters of Eqs. (2) and (3) are determined by solving the set of equations expressed in Eqs. (4)–(20) in externally stress-free configuration as well as under pure glide shear Σ_{23} and the superimposed equal magnitude $\Sigma_{23} + \Sigma_{21}$ and $\Sigma_{23} + \Sigma_{13}$ stress states in dislocation frame.

	Stress-Free	Σ_{23}	$\Sigma_{23} + \Sigma_{21}$	$\Sigma_{23} + \Sigma_{13}$
x_1	0.5	2.1	1.4	2.45
x_2	-0.5	-0.2	-0.4	-0.1
y_1	0.5	1.5	0.8	2.80
y_2	-0.5	-1.5	-0.8	-2.80
α_1	0.5	0.7	0.7	0.86
α_2	0.5	0.3	0.3	0.14
α_3	0.5	0.5	0.5	0.5
α_4	0.5	-0.5	-0.5	-0.5
ξ_1	0.35	1.25	1.15	1.45
ξ_2	0.35	1.15	1.05	2.48
c_1	2.8	5.8	3.3	6.4
c_2	2.8	9.0	3.8	9.6
c_3	2.8	6.0	3.10	3.74
c_4	2.8	6.0	3.10	3.74
CRSS (MPa)	–	174.3	263.7	112.8

that the core widens and the maximum of $\rho_1(x)$ decreases to 0.06 b at $x = 0.5$ b. The spreading of the core structure suggests the planarity of the slip disregistry which complies with the absence of non-glide stress components. Furthermore, it is noted that the peak

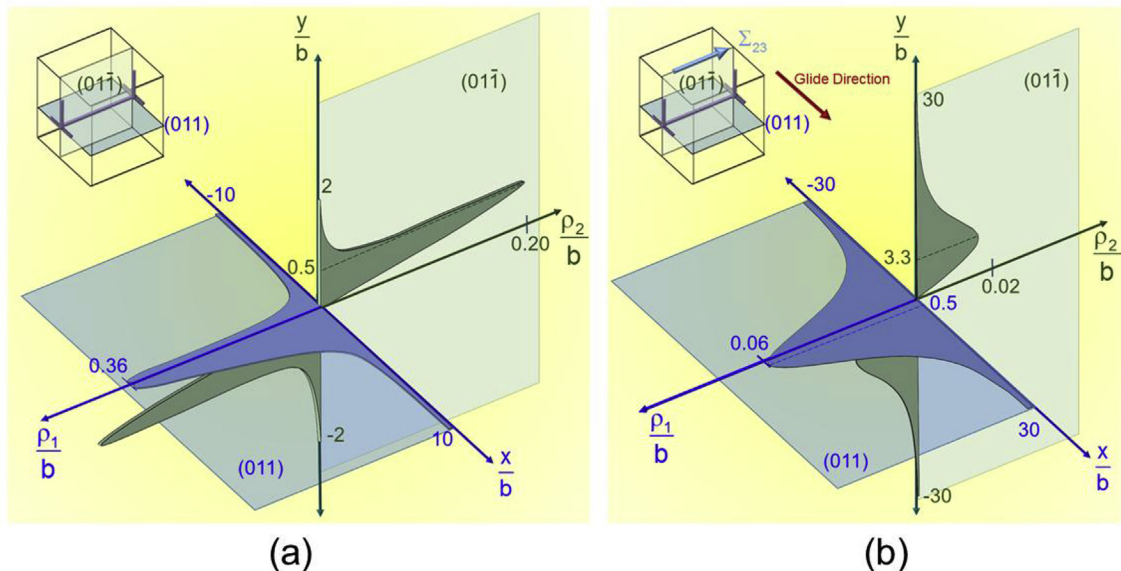


Fig. 9. (a) shows the spatial distribution of infinitesimal dislocation densities $\rho_1(x)$ and $\rho_2(y)$ on the active and conjugate slip planes in stress-free configuration. (b) shows the $\rho_1(x)$ and $\rho_2(y)$ functions at the onset of slip under pure glide shear stress, Σ_{23} .

value of $\rho_1(x)$ has shifted from $x=0$ to $x=0.5b$ position in glide sense. As can be seen, on the conjugate $\{110\}$ plane, the edge character dislocation density diminishes to a peak value of $\rho_2(3.3b)=0.017b$ with an anti-symmetric shape across the active glide plane. This suggests that the edge character displacements are suppressed at the onset of slip promoting the core planarity.

In two distinct scenarios, upon the non-glide stresses Σ_{21} and Σ_{13} , the equal magnitude of glide shear stress Σ_{23} is imposed to initiate glide motion defined as the instability of E^{total} expression. Fig. 10 (a) and (b) show the dislocation core configurations under the superimposed action of $\Sigma_{21} + \Sigma_{23}$ and $\Sigma_{13} + \Sigma_{23}$ respectively (the imposed proportional loading conditions $\Sigma_{21} = \Sigma_{23}$ and $\Sigma_{13} = \Sigma_{23}$). The action of non-glide Σ_{21} stress component opposing to the glide degrades the slip tendency as reflected in Fig. 10 (a) by the greater peak of the screw character dislocation density $\rho_1 : \rho_1(x)$ within the core region compared to the action pure Σ_{23} component in Fig. 9 (b). Similarly, the edge character symmetric $\rho_2 : \rho_2(y)$ density distribution exhibits also a greater peak value suggesting that the promoted edge fractionals which impart additional glide resistance diminishing the extent of core planarity.

In Fig. 10 (b), the dislocation density distributions of $\rho_1(x)$ and $\rho_2(y)$ exhibit lower peak levels with wider core regions ($c_i \xi_i$) under $\Sigma_{13} + \Sigma_{23}$ compared to the pure glide shear case in Fig. 9 (b) which suggests a lower theoretical CRSS value as tabulated in Table 6. To that end, Σ_{13} stress component superimposed up on pure glide component Σ_{23} promotes dislocation glide suppressing the edge character disregistry distribution and facilitating planar configuration.

After establishing the individual contribution of Σ_{23} , Σ_{21} and Σ_{13} shear stress components on the glide resistance of $\{110\} \langle 100 \rangle$ slip system in NiTiCu, we focus our theoretical efforts on the anisotropic variation of CRSS for more complicated stress tensors, tabulated in Tables 4 and 5, applied on the single crystal samples under uniaxial tension and compression in the experiments. Following the theoretical framework introduced by Eq. (4) to Eq. (20), the calculated theoretical CRSS levels are plotted in Fig. 11 (a) employing projection pole angle θ . The theoretical predictions are in well agreement with the experimental measurements. For visualizing the effect of Cu content, we also included the CRSS levels of 50.8% (at.) Ni-Ti alloy in Fig. 11 (b).

3.3. Construction of a generalized yield criterion

The interplay between the non-glide stress components and the non-planar core displacements expressed by $f_1 : f_1(x)$ and $f_2 : f_2(y)$ functions introduce strong deviations from Schmid law. Therefore, a generalized yield criterion which can embrace the contribution of non-glide stresses on the CRSS for slip in NiTiCu should be established. Considering that the hydrostatic portion of the applied stress tensor within the range of experimentally measured stress levels have negligible effect similar to the transformation response of NiTi-based alloys [14,58], we developed a formulation based on the deviatoric stress tensor, S , components corresponding to the onset of slip at the experiments under uniaxial loading along $\langle hkl \rangle$ as $(i,j,m = 1,2,3)$:

$$S_{ij} = \Sigma_{ij}^{hkl} - 1/3 \Sigma_{mm}^{hkl} \delta_{ij} \quad (21)$$

The deviatoric stress tensor S is of zero trace, i.e. $S_{mm} = 0$, and therefore the complete symmetric stress tensor contributing to the CRSS value can be expressed by five independent components of S tensor, namely S_{23} , S_{11} , S_{22} , S_{21} , S_{13} . Based on this rationale, we established the generalized yield criterion of Eq. (21) [14,59,60] in which τ^* , a_1 , a_2 , a_3 and a_4 are the free parameters:

$$\tau^* = CRSS + a_1 S_{11} + a_2 S_{22} + a_3 S_{21} + a_4 S_{13} \quad (22)$$

The yield surface parameters are determined by the multi-linear regression of the experimental measurements of applied stress components tabulated in Tables 4 and 5. The resulting values of these parameters are tabulated in Table 7. As can be seen, the non-Schmid stress components, i.e. the components other than Σ_{23}^{hkl} or equally S_{23} , have finite contribution to the plastic glide resistance exhibiting non-Schmid behavior. Among these components, complying with the theoretical framework, Σ_{21}^{hkl} acting (or equally S_{21}) in an opposite direction to the glide force, i.e. $F_i = -\varepsilon_{ijr} \Sigma_{jm}^{hkl} \zeta_m$ with ε_{ijr} and ζ_m being the components of third order alternating tensor and the unit dislocation line vector in RH/FS convention respectively, promotes the CRSS levels. The edge character fractional dislocation density $\rho_2 = \rho_2(y)$ plays a key role in this behavior. In contrast, Σ_{13}^{hkl} (or S_{13}) stress component which acts parallel to the Burgers vector facilitates slip verifying the

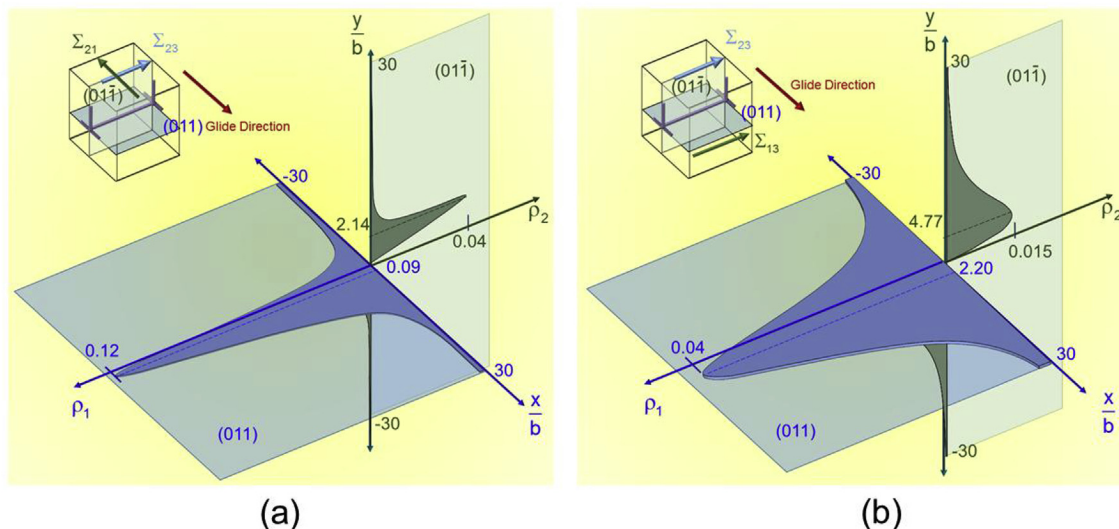


Fig. 10. (a) shows the spatial distribution of infinitesimal dislocation densities $\rho_1(x)$ and $\rho_2(y)$ on the active and conjugate slip planes under superimposed $\Sigma_{23} + \Sigma_{21}$ stress (b) shows the $\rho_1(x)$ and $\rho_2(y)$ functions at the onset of slip under superimposed $\Sigma_{23} + \Sigma_{13}$ stress.

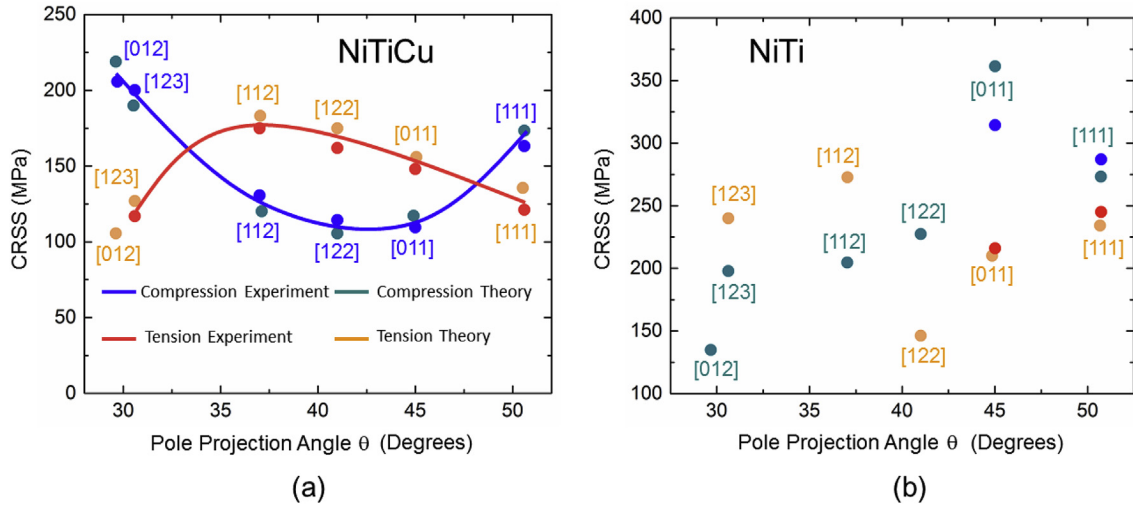


Fig. 11. (a) The theoretical predictions and the experimental measurements of CRSS levels in NiTiCu alloy along $\{110\} \langle 100 \rangle$ slip system under tension and compression for varying crystallographic orientations are plotted. (b) The theoretical predictions and the experimental measurements of CRSS levels in NiTi alloy along $\{110\} \langle 100 \rangle$ slip system under tension and compression for varying crystallographic orientations are plotted.

Table 7

Shows the yield surface parameters describing the onset of plastic slip in NiTiCu alloy in deviatoric stress space are tabulated.

τ^* (MPa)	a_1	a_2	a_3	a_4
162.3	-0.66	-0.65	-0.40	0.50

theoretical trends. Furthermore, the normal deviatoric stress components, S_{11} and S_{22} , have a prominent effect on the resulting CRSS magnitude.

In order to visualize the effect of non-glide stress components from a broader perspective, we generated the generalized yield surface in the principal stress space which is basically the projection of the yield hypersurface on the π plane with a unit normal of $1/\sqrt{3}$ [111]. To accomplish this task, we parameterized the principal stress components $\sigma_1 = \alpha \sin \psi \cos \phi$, $\sigma_2 = \alpha \sin \psi \sin \phi$ and $\sigma_3 = \alpha \cos \phi$ where α is the proportionality constant and the azimuthal angles, ψ and ϕ , range in an interval of $[0, \pi]$ and $[0, 2\pi]$

respectively with an incremental step of 0.01° . These principal stress components are substituted into Eq. (22) with the corresponding deviatoric stress components and the resulting yield locus of NiTiCu alloy is plotted in Fig. 12(a). For comparison purposes, the NiTi alloy yield locus is also included in Fig. 12 (b) [15]. As can be seen, the yield locus of NiTiCu alloy exhibits strong anisotropy addressing the contribution of non-Schmid stress components which introduce both tension-compression asymmetry and orientation dependence in CRSS levels. Careful examination of NiTiCu yield locus suggests a maximum theoretical difference of almost 450 MPa based on the loading orientation.

In the present work, the extent of anisotropy pertinent to the yield loci for NiTiCu and NiTi are quantified based on a novel parameter η which incorporates both the angular deviations from the six-fold symmetric Schmid law obeying yield surface and the size of the elastic regime as follows:

$$\eta = \frac{1}{h_0 2\pi} \max \left\{ h_{ij} \left(\left| \theta_i - \frac{2\pi}{3} \right| + \left| \theta_j - \frac{2\pi}{3} \right| \right) \right\} \quad (23)$$

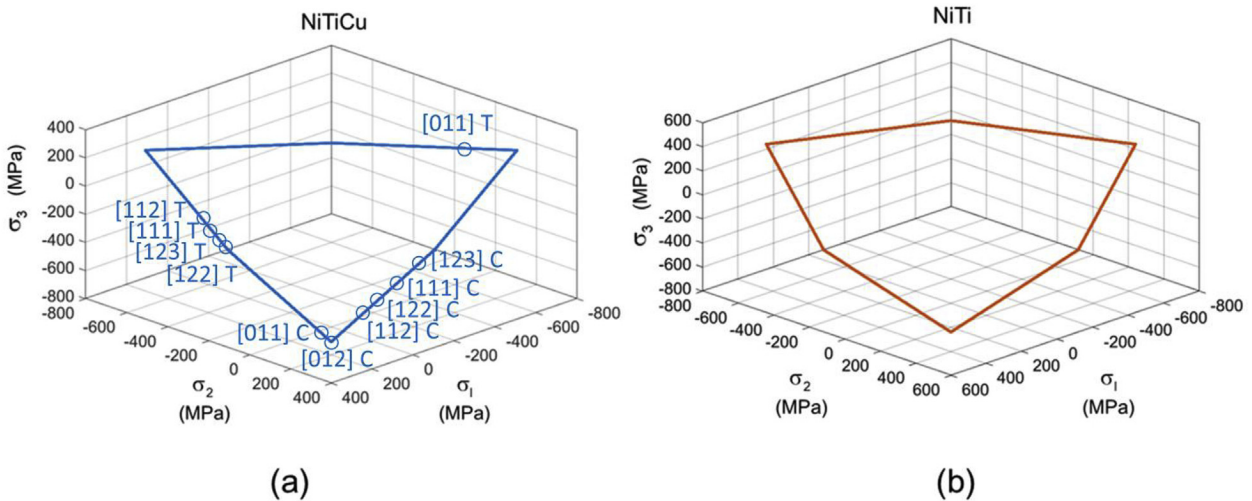


Fig. 12. (a) shows the generalized yield surface based on Eq. (22) for NiTiCu in principle stress space. (b) For comparison purposes, the generalized yield surface of NiTi alloy is also plotted in principal stress space. As can be seen both shape memory alloys exhibit strong anisotropy in plastic slip resistance.

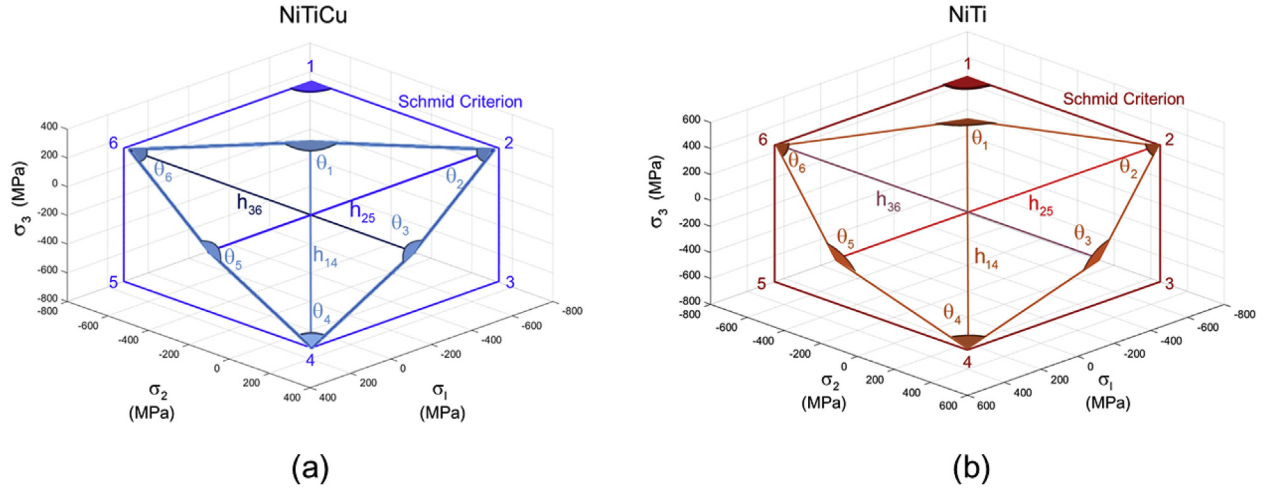


Fig. 13. (a) compares the yield surfaces of NiTiCu based on generalized yield criterion proposed in Eq. (22) and the Schmid criterion showing the interior angles θ_i and the distance measures h_{ij} ($i, j = 1$ to 6) in principal stress space. (b) compares the yield surfaces of NiTi based on generalized yield criterion and the Schmid criterion showing the interior angles θ_i and the distance measures h_{ij} ($i, j = 1$ to 6) in principal stress space.

In Eq. (23), the indices i, j vary from 1 to 6, the internal angles θ_i and θ_j represent the opposite interior angles separated by a distance h_{ij} . The normalizing factor h_0 is taken as 1000 MPa. Meanwhile the sum of the deviation of the opposite interior angles from $2\pi/3$ represents the distortion of the yield surface shape from the six-fold symmetric Schmid law, multiplying it with the factor of h_{ij} distance conveys information for the tension-compression asymmetry as demonstrated in Fig. 13. It is to be noted that $\eta = 0$ indicates the validity of Schmid law. Within this framework, the η parameter corresponds to 0.52 and 0.32 for NiTiCu and NiTi respectively. Considering this quantitative analysis, the slip resistance in NiTiCu stands out to be more anisotropic than NiTi.

The construction of the generalized yield surface for NiTiCu alloy allows us to incorporate the contribution of non-glide and glide stresses on critical flow stress; however, a more specific description under uniaxial tension and compression loading can be also developed modifying the concept of Schmid factor, P . On geometrical grounds, the factor P describes the resolved shear stress along a slip system under unit magnitude uniaxial loading. For a potential slip system of a unit plane normal \mathbf{n} , and a unit slip direction, \mathbf{m} , the resolved shear stress τ corresponds to:

$$\tau = \mathbf{P} : \mathbf{S} \quad (24)$$

where $(:)$ is the inner product operator and the Schmid tensor, \mathbf{P} , is expressed as:

$$\mathbf{P} = \frac{1}{2}(\mathbf{n} \otimes \mathbf{m} + \mathbf{m} \otimes \mathbf{n}) \quad (25)$$

in which (\otimes) stands for the outer product operator. It is to be noted, for an active slip system, the vectors \mathbf{n} and \mathbf{m} coincide with the dislocation frame base vectors \mathbf{e}_2 and \mathbf{e}_3 visualized in Fig. 2 respectively. Within the framework of Schmid law, the resolved shear stress τ is equal to a constant CRSS level, τ_{cr} , irrespective of the applied stress state such as:

$$\tau_{cr} = \tau \quad (26)$$

Similarly, a modified Schmid tensor, \mathbf{P}_{mod} , can be also defined to embrace the generalized yield criterion in which CRSS levels vary as a function of both glide and non-glide deviatoric stress components as such:

$$\mathbf{P}_{mod} = \mathbf{P} + a_1(\mathbf{n} \times \mathbf{m}) \otimes (\mathbf{m} \times \mathbf{n}) + a_2 \mathbf{n} \otimes \mathbf{n} + a_3 \mathbf{n} \otimes (\mathbf{n} \times \mathbf{m}) + a_4(\mathbf{n} \times \mathbf{m}) \otimes \mathbf{m} \quad (27)$$

where (\times) is the vector cross-product operator. The inner product of \mathbf{P}_{mod} with the deviatoric portion of the applied stress, i.e. \mathbf{S} , satisfies the generalized yield criterion Eq. (22) at the onset of slip:

$$\tau^* = \mathbf{P}_{mod} : \mathbf{S} \quad (28)$$

These geometric definitions allow us to incorporate the contribution of non-glide stresses on yielding under uniaxial loading via \mathbf{P}_{mod} tensor. To this end, the modified Schmid factor P_{mod} is defined as:

$$P_{mod} = \mathbf{v} \cdot \mathbf{P}_{mod} \mathbf{v} \quad (29)$$

where the unit vector \mathbf{v} is parallel to \mathbf{E}_2 base vector in sample frame (i.e. along specimen loading axis direction) and (\cdot) is the vector dot product operator. Similarly, the Schmid factor P is also expressed as:

$$P = \mathbf{v} \cdot \mathbf{P} \mathbf{v} \quad (30)$$

The scalar factors P_{mod} and P are especially instrumental in case they are mapped on the stereographic triangle as shown in Fig. 14. As can be seen in Fig. 14 (a) and (b), the factor P_{mod} behaves significantly different under uniaxial tension and compression as the generalized yield criterion predicts distinct CRSS levels in these cases complying with the experimental data. In contrast, the Schmid factor P behaves identical under tension and compression. The stereographic mappings in Fig. 14 also demonstrate that significant differences emerge between Schmid law and the generalized yield criterion owing to the interplay among the non-glide stresses and dislocation core displacements. Meanwhile Schmid law predicts an easy-glide zone located near the $[111]$ pole on the stereographic triangle as shown in Fig. 14 (c), close proximity of the $[011]$ pole under compression and the $[123]$ direction under tension exhibit low glide resistance according to the generalized yield criterion in NiTiCu. This difference emphasizes the fact that the Schmid factor, P , is derived based on the geometrical arguments independent of the material properties. On the other hand, the modified Schmid factor, P_{mod} , is unique for a particular material as the anisotropic variation of CRSS levels is governed by the interaction between the non-glide stresses and the dislocation core

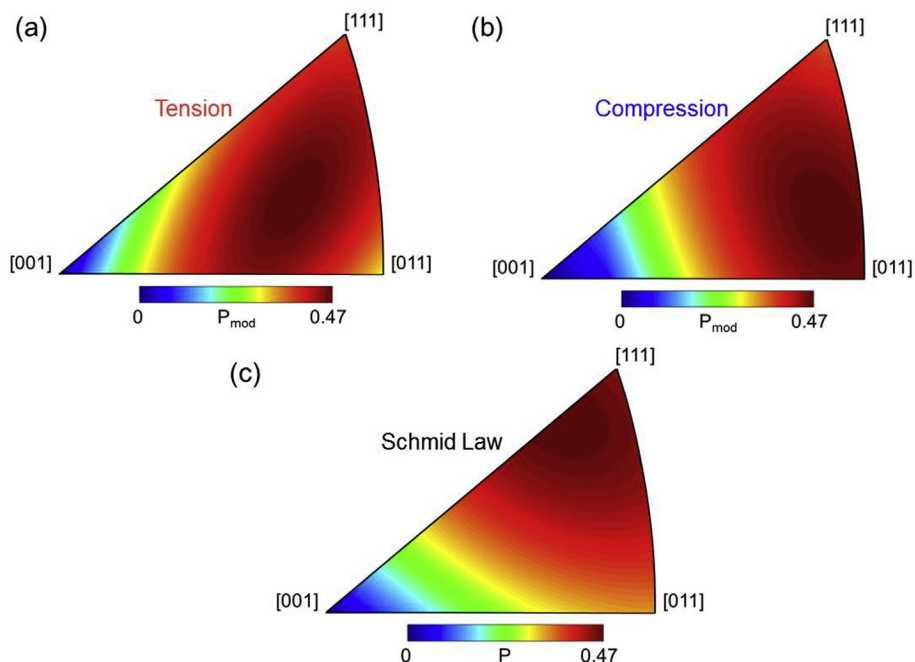


Fig. 14. (a) shows the modified Schmid factor distribution P_{mod} on the stereographic triangle under tension in NiTiCu for $\{110\}$ $\langle 100 \rangle$ system. (b) shows the distribution of P_{mod} on the stereographic triangle under compression in NiTiCu for $\{110\}$ $\langle 100 \rangle$ system. (c) shows the distribution of Schmid factor P on the stereographic triangle for $\{110\}$ $\langle 100 \rangle$ system. The P factor does not distinguish the tension-compression asymmetry unlike P_{mod} .

disregistry displacements. This interaction involves elastic properties and the GSFE profile of a given material along the active slip system.

4. Discussion of results

The lower glide resistance of NiTiCu compared to the binary NiTi alloy is reflected by the diminishing effect of Cu on γ^{us} levels of NiTiCu and NiTi which are 185 mJ/m² and 200.5 mJ/m² respectively. Previous work on plasticity of shape memory alloys recognized the deleterious effect of lower CRSS for slip compared to the transformation stress particularly as the dislocations accommodating the corresponding large mismatch strains at the austenite - martensite interfaces give rise to the irreversible strains emerging under cyclic loading [7,17,61–64]. The experimental measurements by Strnadel et al. [17] exemplify that the slip accompanying the pseudoelastic cycling is of substantial significance in the rapid decline of the martensitic transformation stress in NiTi and NiTiCu shape memory alloys. The lowering of forward transformation stress is expected to result from the interaction of dislocations located inside the austenite phase and the martensite transformation front which in turn hinders the cyclic interphase motion leading to retained martensite plates [11]. Consistently, these retained martensite plates are likely to act as pre-existing local nucleation sites for the transformation [11,65,66].

Contrasting with its prominent role in functional properties of NiTiCu, the magnitude of stress at the onset of dislocation glide motion has not been determined previously in a theoretical basis. As shown in Figs. 11–14, the high anisotropy involved in NiTi based ordered shape memory alloys exhibit anisotropic CRSS levels with tension-compression asymmetry. The Schmid law, suggesting a single parameter representation of the plastic glide resistance in NiTiCu, is deficient as CRSS for slip strongly depends on the complete stress state. The present study demonstrates the contribution of non-glide stress components on the CRSS for slip in Figs. 9 and 10. On experimental grounds, the non-glide shear stress of Σ_{21}

has been observed to promote the CRSS levels if it is directed along an opposite sense to the glide force applied by the glide shear stress of Σ_{23} and vice versa. On the other hand, the shear stress of Σ_{13} is measured to facilitate the glide if it exerts a glide force magnifying the glide force of Σ_{23} . This effect plays a prominent role in tension-compression asymmetry exhibited by the values of CRSS for slip in NiTiCu.

The continuum modelling of dislocations [67] lacks a satisfactory explanation for the discrepancies from Schmid law. This serves as a motivation in propelling the theoretical efforts towards the atomistic scale description of screw dislocation core structures which are known to exhibit non-planar spreading in bcc derivative lattices including B2 ordered austenitic NiTiCu. Close examination of theoretical predictions reveal the dislocation core structure modelling framework engenders a close agreement with the experimental measurements. The results are noteworthy as the CRSS levels exhibit high anisotropy which shed light on the effects of edge character disregistry fields. Meanwhile, the resultant of these edge disregistry fields is zero for a screw dislocation, they contribute substantially to the non-planar sessile to planar glissile core transformation by interacting with the non-glide stress components. These local edge character displacements do not contribute to the net Peach-Koehler force based work definition within the framework of Schmid law [68]. Consequently, a more sophisticated description of the yielding criterion is necessary to address in a wide range of problems with SMAs including deformation under different stress states, fatigue response and changes in functionality of these alloys.

Comparison of the CRSS levels for slip under varying single crystal orientations in tension and compression reveals that [011] compression sample exhibits a lower glide resistance by a magnitude of almost 100 MPa differential compared to the [012] compression sample. Considering the earlier works on the functional performance of NiTiCu alloys [19,41], this glide strength differential among different sample orientations can explain the high recovery ratios of transformation strain for [012] loading

orientation compared to [011] sample under compression. This result exemplifies the paramount importance of anisotropic glide resistance in optimizing the functional performance of NiTiCu which is influential in suppressing the slip in the austenite phase during martensitic transformation. Similarly, the higher transformation strain in [122] sample compared to [111] sample under tension is closely linked with the higher CRSS of [122] sample as demonstrated in Fig. 11.

Detailed electronic configuration analyses show that the Zener anisotropic ratio, i.e. defined as $A = 2C_{44}/(C_{11} - C_{12})$, is greater in Ni_{43.25}Ti₅₀Cu_{6.25} (which is a very similar composition compared to the ternary NiTiCu alloy employed in the present study) than NiTi which are 5.2 and 2.4 respectively [57]. Meanwhile, A ratio is known to play a key role in the difference of the transformation paths of solutionized NiTiCu (i.e. B2-B19 and B19-B19') and NiTi (i.e. B2-B19') [69], the generalized yield surfaces of the alloys in Fig. 12 suggest that it might also act as a significant parameter in slip mediated plasticity in these SMAs. Considering the fact that A ratio is a metric for describing the anisotropy of the crystal structure, the more pronounced deviations from Schmid law in NiTiCu than NiTi are surmised to be correlated with the orientation dependent nature of the interatomic forces governing on elastic stiffness tensor components. This pronounced anisotropy is also persistent in polycrystalline samples, i.e. $A = 2.02$ and 1.32 for NiTiCu and NiTi respectively [70]. To this end, deviations from Schmid law are also expected in the presence of grain boundaries which act as a motivation for the prospective studies. The quantification of the anisotropy involved in the yield loci has been an attractive topic in the community [71–74]. Yield criteria aiming to capture strength differentials between tension and compression as a result of asymmetric slip or twin mediated plasticity has been proposed for polycrystalline materials within the framework of homogeneous stress functions expressed in terms of odd power second and third invariants of deviatoric stress tensor, namely J₂ and J₃ [73]. On the other hand, the generalized criteria capturing the deviations from Schmid law for symmetric glide systems as in the particular case of {110} <100> family has yet to be established in the literature. As an example, for NiTiCu and NiTi [14,15], the presence of the non-glide stress components acting on the non-planar dislocation cores is shown to introduce significant deviations from Schmid law.

In the present work, we introduce a novel dimensionless parameter η which acts as a measure of the anisotropic CRSS differentials between the generalized and Schmid law based yield loci. The geometrical parameter η is composed of two factors: (i) normalized deviations in the interior angles of θ_i , (ii) the normalized distances between the opposite corners h_{ij} . Meanwhile, the angular deviations depict the distortion of the generalized yield surface due to the non-glide stress terms in distinct crystal orientations, the distance differentials quantify the contribution of the tension-compression asymmetry. The direct comparison between the generalized yield surfaces resulted in the fact that η is greater for NiTiCu compared to NiTi, 0.52 and 0.32 respectively. This result points that even though the glide resistance is greater in NiTi, NiTiCu behaves in a more anisotropic fashion at the instant of slip activation. To this end, both elastic and plastic anisotropy in NiTiCu has been shown to be greater than NiTi.

Meanwhile dislocation glide plays a key role in accommodating the plastic deformation, deformation twinning can also occur at higher stresses on the {114}<112> system in NiTi based shape memory alloys [75,76]. Therefore, deformation twinning impart additional ductility to NiTiCu alloy in austenitic regime. Because the CRSS for twinning is near 200 MPa in these alloys based on our experimental measurements, the slip-mediated plastic flow dominates for the strain ranges studied except the [001] compression sample. In [001] compression sample, the deformation twinning

initiates before slip which is expected on geometrical grounds considering the zero Schmid factor, P, along the {110}<100> slip system. On the other hand, [001] tension sample fails due to cleavage along the (001) plane which is prevalent in brittle fracture of bcc based intermetallics [28]. We also note that experiments at various temperatures were conducted in this study. The local orientations were monitored with EBSD to ensure that we are reporting stress levels corresponding to plastic flow in this study and not stress-induced martensite or mechanical twinning.

According to the crystallographical theory of martensite, the improved compatibility is closely linked with the principal stretch values. For the cases in which the median principal stretch value λ , being close to 1 with negligible volume change during transformation, a high level of lattice correspondence between the austenite and martensite phases across the habit plane is predicted on crystallographical grounds [77,78]. From this perspective, comparison of NiTi and NiTiCu alloys imply superior fatigue properties for the latter case [18,20]. Considering the contribution of transformation-induced dislocations located on interphase boundaries to the cyclic irreversibility, the higher interphase compatibility in NiTiCu can lead to a lower density of dislocation networks. However, further experimental evidence including high resolution transmission electron microscopy studies are necessary to establish a firmer understanding for the effect of Cu addition on the mechanical behavior of NiTi based shape memory alloys. On the other hand, the anisotropic variation of the functional performance in these two alloys and the CRSS magnitudes support the superiority of NiTi compared to NiTiCu.

We note that the conventional characteristic MRSSP angle description employed for interrogating the anisotropy involved in the CRSS levels of bcc metals fails to correspond to a one to one relationship in a number of orientations residing at the edges of the standard inverse pole figure. Instead, a new pole angle of θ is proposed that provides a smooth variation of the CRSS as a function of orientation. The reason for the success of the pole projection description is three fold: (i) bijective relationship between the orientation and the CRSS levels are accomplished among the chosen single crystal orientations. For example, both [012] and [011] orientations correspond to $\chi = 45^\circ$ for the active system of <001> {110} meanwhile they are distinguished by $\theta = 29.7^\circ$ and $\theta = 45^\circ$ in the novel θ angle convention. (ii) the resulting geometrical description allows to assess data irrespective of the slip system for the same material in a single figure (the active glide system can belong either to <001>{110}, <111>{110} or <111>{112} families in bcc based materials). (iii) direct geometrical conversion between the conventional and the novel conventions is easily established. To this end, the core disregistry distributions and the CRSS levels on the active glide systems can be directly compared for different orientations without distinguishing the crystallographic indices of the active slip system in the same material.

It is important to emphasize that in addition to the lower levels of anisotropic plastic glide resistance in NiTiCu in contrast to its high transformation strain potential, the following mechanical and chemical factors also put limitations on the common use of this SMA: (i) the two step transformation path introduces interactions between the distinct transformation domains of B19 and B19' potentially leading to irreversibility under cyclic loading, (ii) the low cold-work capacity limits its deformability, (iii) low corrosive resistance associated with its ion release characteristics requires to exclude its use in medical applications. During shape-setting at ambient air, the formation of Ti₄(Ni,Cu)₂O_x oxide impurities play a key role in the mechanical of NiTiCu [21]. The emergence of oxide layers along the grain boundaries in as-cast structures introduces brittle behavior and stands out as a potential failure mechanism limiting the use of NiTiCu in polycrystalline applications.

Furthermore, the release of Cu ions is observed to lead high cytotoxicity limiting the use of NiTiCu in biomedical applications [79]. Finally, we comment on the future studies with NiTiCu alloys. The lower slip resistance compared to NiTi alloys is noted as a shortcoming of NiTiCu alloys. For textured crystals near the [111] pole, the flow stress of NiTiCu is nearly a factor of 2 smaller compared to NiTi. Furthermore, the degree of anisotropy of the flow stress is higher in NiTiCu compared to the NiTi. From these theoretical simulations, we have been able to discern the decrease in flow stress with addition of Cu without any assumptions or empirical constants. On the other hand, a nearly twinless martensite phase in NiTiCu is expected to lower the transformation stress. Similarly, the interplay between the transformation and slip in cold-worked polycrystalline samples necessitate a detailed analysis on the deformation behavior of interfaces. Therefore the NiTiCu may find niche applications with lower transformation stress despite the lower plastic flow resistance. This is left for future studies.

5. Conclusions

The results suggest the following conclusions on the slip resistance of NiTiCu:

The CRSS levels for slip are measured to exhibit strong anisotropy in NiTiCu as a function of single crystal orientation under uniaxial tension and compression in NiTiCu.

The theoretical model demonstrates that the interplay of the glide and non-glide applied stress components with the non-planar screw dislocation core structure plays a major role in the non-Schmid behavior of CRSS for slip.

Theoretical predictions conform to the experiments conducted on single crystals which show that the CRSS levels vary in the range of 100–200 MPa as a function of sample orientation. The maximum slip resistance is lower compared to NiTi (300 MPa) and similar to CuZnAl (200 MPa).

A generalized yield criteria is proposed for NiTiCu which shows substantial departure from the commonly used Schmid law. Comparison between NiTi and NiTiCu reveals that the slip strength levels for NiTiCu alloy are lower. On the other hand, the degree of both elastic and plastic anisotropy is greater in NiTiCu than NiTi. This results in a higher propensity for plastic flow that could adversely affect the shape memory functionality.

Acknowledgements

The support of Nyquist Chair funds and the National Science Foundation, DMREF grant # 1437106 are gratefully acknowledged. The assistance of Mr. Sidharth Ravi and Mr. Yan Wu on the experiments are gratefully acknowledged.

References

- [1] H. Funakubo, Shape Memory Alloys, Gordon and Breach Science Publishers, 1987 translated from the Japanese by J.B. Kennedy.
- [2] K. Otsuka, C.M. Wayman (Eds.), Shape Memory Materials, Cambridge University Press, Cambridge, 1998.
- [3] L.C. Chang, T.A. Read, The gold-cadmium beta phase, *Trans. AIME* 191 (1951) 47.
- [4] C.M. Wayman, I. Cornelis, K. Shimizu, Transformation behavior and the shape memory in thermally cycled TiNi, *Scripta Metall.* 6 (1972) 115–122.
- [5] S. Miyazaki, K. Otsuka, Y. Suzuki, Transformation pseudoelasticity and deformation behavior in a Ti-50.6at%Ni alloy, *Scripta Metall.* 15 (1981) 287–292.
- [6] T.W. Duerig, K. Melton, D. Stockel, C. Wayman, Engineering Aspects of Shape Memory Alloys, Butterworth-Heinemann, Reed Books Services Ltd, P. O. Box 5, Rushden, Northants, NN 10 9 YX, UK, 1990, 1990, 499.
- [7] P. Chowdhury, H. Sehitoglu, A revisit to atomistic rationale for slip in shape memory alloys, *Prog. Mater. Sci.* 85 (2017) 1–42.
- [8] P. Chowdhury, H. Sehitoglu, Deformation physics of shape memory alloys – fundamentals at atomistic frontier, *Prog. Mater. Sci.* 88 (2017) 49–88.
- [9] D.C. Lagoudas, Shape Memory Alloys: Modeling and Engineering Applications, Springer, 2008.
- [10] R.F. Hamilton, H. Sehitoglu, Y. Chumlyakov, H.J. Maier, Stress dependence of the hysteresis in single crystal NiTi alloys, *Acta Mater.* 52 (2004) 3383.
- [11] R. Delville, B. Malard, J. Pilch, P. Sittner, D. Schryvers, Transmission electron microscopy investigation of dislocation slip during superelastic cycling of Ni–Ti wires, *Int. J. Plast.* 27 (2011) 282–297.
- [12] T. Simon, A. Kroger, C. Somsen, A. Dlouhy, G. Eggeler, On the multiplication of dislocations during martensitic transformations in NiTi shape memory alloys, *Acta Mater.* 58 (2010) 1850–1860.
- [13] W.Y. Sehitoglu, H. Alkan, S. Ertekin, E. Plastic Deformation of B2-niti- Is it Slip or Twinning?, (To Appear in Philosophical Magazine Letters).
- [14] S. Alkan, H. Sehitoglu, Dislocation core effects on slip response of NiTi- a key to understanding shape memory, *Int. J. Plast.* 97 (2017) 126–144.
- [15] S. Alkan, Y. Wu, H. Sehitoglu, Giant non-Schmid effect in NiTi, *Extreme Mechanics Letters* 15 (2017) 38–43.
- [16] W. Moberly, J. Proft, T. Duerig, R. Sinclair, Twinless martensite in TiNiCu shape memory alloys, *Mater. Sci. Forum* 56 (1989) 605–610.
- [17] B. Strnadel, S. Ohashi, H. Ohtsuka, S. Miyazaki, T. Ishihara, Effect of mechanical cycling on the pseudoelasticity characteristics of Ti–Ni and Ti–Ni–Cu alloys, *Mater. Sci. Eng., A* 203 (1995) 187–196.
- [18] C. Grossmann, J. Frenzel, V. Sampath, T. Depka, G. Eggeler, Elementary transformation and deformation processes and the cyclic stability of NiTi and NiTiCu shape memory, *Spring Actuators, Metallurgical and Materials Transactions A* 40 (2009) 2530.
- [19] H. Sehitoglu, I. Karaman, X. Zhang, A. Viswanath, Y. Chumlyakov, H.J. Maier, Strain–temperature behavior of NiTiCu shape memory single crystals, *Acta Mater.* 49 (2001) 3621–3634.
- [20] S. Miyazaki, My experience with Ti–Ni-based and Ti-based shape memory alloys, *Shape Memory and Superelasticity* 3 (2017) 279–314.
- [21] T.W. Duerig, K.N. Melton, D. Stockel, Engineering Aspects of Shape Memory Alloys, Elsevier Science, 2013.
- [22] M.S. Wechsler, D.S. Lieberman, T.A. Read, On theory of formation of martensite, *J. Met.* 5 (1953) 1503–1515.
- [23] M.S. Duesbery, The dislocation core and plasticity, in: F.R.N. Nabarro (Ed.), *Dislocations in Solids*, vol. 8, Elsevier Science Publishers B.V., Netherlands, 1989, pp. 67–173.
- [24] V.V. Bulatov, E. Kaxiras, Semidiscrete variational Peierls framework for dislocation core properties, *Phys. Rev. Lett.* 78 (1997) 4221–4224.
- [25] E. Schmid, W. Boas, Plasticity of Crystals, A.Hughes and Co., London, 1950.
- [26] R. Hill, The Mathematical Theory of Plasticity, Oxford university press, 1998.
- [27] R.J. Asaro, Crystal plasticity, *J. Appl. Mech.* 50 (1983) 921–934.
- [28] N. Hatcher, Electronic and Phononic Origins of Martensitic Behavior in Nickel Titanium-based Binary and Ternary Shape Memory Alloys, 2010.
- [29] H.Y. Kim, Y. Yuan, T.-H. Nam, S. Miyazaki, Effect of Pd content on crystallization and shape memory properties of Ti–Ni–Pd thin films, *Int. J. Soc. Netw. Min.* 2 (2011) 9–21.
- [30] T. Inamura, Y. Takahashi, H. Hosoda, K. Wakashima, T. Nagase, T. Nakano, Y. Umakoshi, S. Miyazaki, Martensitic transformation behavior and shape memory properties of Ti–Ni–Pt melt-spun ribbons, *Mater. Trans.* 47 (2006) 540–545.
- [31] K.H. Eckelmeyer, The effect of alloying on the shape memory phenomenon in nitinol, *Scripta Metall.* 10 (1976) 667–672.
- [32] H. Hosoda, K. Wakashima, S. Miyazaki, K. Inoue, Factors for controlling martensitic transformation temperature of TiNi shape memory alloy by addition of ternary elements, *MRS Proceedings* 842 (2011), S3.4.
- [33] H. Hosoda, S. Hanada, K. Inoue, T. Fukui, Y. Mishima, T. Suzuki, Martensite transformation temperatures and mechanical properties of ternary NiTi alloys with offstoichiometric compositions, *Intermetallics* 6 (1998) 291–301.
- [34] T.H. Nam, T. Saburi, K. Shimizu, R. Sroog, Ichi, Cu-content dependence of shape memory characteristics in Ti–Ni–Cu alloys, *Mater. Trans., JIM* 31 (1990) 959–967.
- [35] V.G. Pushin, N.N. Kuranova, A.V. Pushin, A.V. Korolev, N.I. Kourov, Effect of copper on the structure–phase transformations and the properties of quasi-binary TiNi–TiCu alloys, *Tech. Phys.* 61 (2016) 554–562.
- [36] J. Frenzel, A. Wiczorek, I. Opahle, B. Maaß, R. Drautz, G. Eggeler, On the effect of alloy composition on martensite start temperatures and latent heats in Ni–Ti-based shape memory alloys, *Acta Mater.* 90 (2015) 213–231.
- [37] N.G. Jones, D. Dye, Influence of applied stress on the transformation behaviour and martensite evolution of a Ti–Ni–Cu shape memory alloy, *Intermetallics* 32 (2013) 239–249.
- [38] P. Sedmák, P. Sittner, J. Pilch, C. Curfs, Instability of cyclic superelastic deformation of NiTi investigated by synchrotron X-ray diffraction, *Acta Mater.* 94 (2015) 257–270.
- [39] P. Sedmák, J. Pilch, L. Heller, J. Kopeček, J. Wright, P. Sedlák, M. Frost, P. Sittner, Grain-resolved analysis of localized deformation in nickel-titanium wire under tensile load, *Science* 353 (2016) 559–562.
- [40] H. Morawiec, D. Stróż, T. Goryczka, D. Chrobak, Two-stage martensitic transformation in a deformed and annealed NiTi alloy, *Scripta Mater.* 35 (1996) 485–490.
- [41] T. Kotil, H. Sehitoglu, H.J. Maier, Y.I. Chumlyakov, Transformation and detwinning induced electrical resistance variations in NiTiCu, *Mater. Sci. Eng., A* 359 (2003) 280–289.
- [42] W.J. Moberly, T. Duerig, J. Proft, R. Sinclair, Two-step Martensitic Transformations in TiNi (10% Cu) Shape Memory Alloys, vol. 246, MRS Online

- Proceedings Library Archive, 1991.
- [43] K. Gall, H. Sehitoglu, Y.I. Chumlyakov, I.V. Kireeva, Tension–compression asymmetry of the stress–strain response in aged single crystal and polycrystalline NiTi, *Acta Mater.* 47 (1999) 1203–1217.
- [44] P. Sittner, V. Novák, Anisotropy of Cu-based shape memory alloys in tension/compression thermomechanical loads, *J. Eng. Mater. Technol.* 121 (1999) 48–55.
- [45] J. Christian, Some surprising features of the plastic deformation of body-centered cubic metals and alloys, *Metallurgical Transactions A* 14 (1983) 1237–1256.
- [46] K. Ito, V. Vitek, Atomistic study of non-Schmid effects in the plastic yielding of bcc metals, *Philos. Mag. A* 81 (2001) 1387–1407.
- [47] S. Alkan, H. Sehitoglu, Non-Schmid response of Fe3Al: the twin-antitwin slip asymmetry and non-glide shear stress effects, *Acta Mater.* 125 (2017) 550–566.
- [48] G. Kresse, J. Furthmüller, Efficient iterative schemes for ab initio total-energy calculations using a plane-wave basis set, *Phys. Rev. B* 54 (1996) 11169–11186.
- [49] G. Kresse, J. Hafner, Ab initio molecular dynamics for open-shell transition metals, *Phys. Rev. B* 48 (1993) 13115–13118.
- [50] R.H. Bricknell, K.N. Melton, O. Mercier, The structure of NiTiCu shape memory alloys, *Metallurgical Transactions A* 10 (1979) 693–697.
- [51] J.D. Eshelby, LXXXII. Edge dislocations in anisotropic materials, *The London, Edinburgh, and Dublin Philosophical Magazine and Journal of Science* 40 (1949) 903–912.
- [52] J.D. Eshelby, W.T. Read, W. Shockley, Anisotropic elasticity with applications to dislocation theory, *Acta Metall.* 1 (1953) 251–259.
- [53] F. Kroupa, L. Lejček, Splitting of dislocations in the Peierls-Nabarro model, *Czech. J. Phys. B* 22 (1972) 813–825.
- [54] R. Peierls, The size of a dislocation, *Proc. Phys. Soc.* 52 (1940) 34.
- [55] F.R.N. Nabarro, Dislocation in a simple cubic lattice, *Proc. Phys. Soc.* 59 (1947).
- [56] L. Lejček, F. Kroupa, Peierls-Nabarro model of non-planar screw dislocation cores, *Czech. J. Phys. B* 26 (1976) 528–537.
- [57] C. Tan, W. Cai, J. Zhu, First-principles study on the elastic properties and electronic structure of TiNi-based ternary shape memory alloys, *Phys. Status Solidi* 243 (2006) R69–R71.
- [58] K. Jacobus, H. Sehitoglu, M. Balzer, Effect of stress state on the stress-induced martensitic transformation in polycrystalline Ni-Ti alloy, *Metall. Mater. Trans.* 27 (1996) 3066–3073.
- [59] Q. Qin, J.L. Bassani, Non-schmid yield behavior in single crystals, *J. Mech. Phys. Solid.* 40 (1992) 813–833.
- [60] R. Gröger, V. Racherla, J.L. Bassani, V. Vitek, Multiscale modeling of plastic deformation of molybdenum and tungsten: II. Yield criterion for single crystals based on atomistic studies of glide of $1/2\langle 111 \rangle$ screw dislocations, *Acta Mater.* 56 (2008) 5412–5425.
- [61] E. Hornbogen, Review Thermo-mechanical fatigue of shape memory alloys, *J. Mater. Sci.* 39 (2004) 385–399.
- [62] M. Frotscher, S. Wu, T. Simon, C. Somsen, A. Dlouhy, G. Eggeler, Elementary deformation and damage mechanisms during fatigue of pseudoelastic NiTi microstents, *Adv. Eng. Mater.* 13 (2011) B181–B186.
- [63] Y. Wu, A. Ojha, L. Patriarca, H. Sehitoglu, Fatigue crack growth fundamentals in shape memory alloys, *Shape Memory and Superelasticity* 1 (2015) 18–40.
- [64] A.M. David, C.L. Dimitris, Thermomechanical characterization of NiTiCu and NiTi SMA actuators: influence of plastic strains, *Smart Mater. Struct.* 9 (2000) 640.
- [65] K. Gall, H. Sehitoglu, Y.I. Chumlyakov, I.V. Kireeva, Pseudoelastic cyclic stress-strain response of over-aged single crystal Ti-50.8at%Ni, *Scripta Mater.* 40 (1998) 7–12.
- [66] T. Simon, A. Kröger, C. Somsen, A. Dlouhy, G. Eggeler, On the multiplication of dislocations during martensitic transformations in NiTi shape memory alloys, *Acta Mater.* 58 (2010) 1850–1860.
- [67] J.P. Hirth, J. Lothe, *Theory of Dislocations*, 2 ed., Krieger Pub. Co., 1992.
- [68] R. Hill, J.R. Rice, Constitutive analysis of elastic-plastic crystals at arbitrary strain, *J. Mech. Phys. Solid.* 20 (1972) 401–413.
- [69] X. Ren, N. Miura, J. Zhang, K. Otsuka, K. Tanaka, M. Koiwa, T. Suzuki, Y.I. Chumlyakov, M. Asai, A comparative study of elastic constants of Ti–Ni-based alloys prior to martensitic transformation, *Mater. Sci. Eng., A* 312 (2001) 196–206.
- [70] M. Thomasová, H. Seiner, P. Sedláč, M. Frost, M. Ševčík, I. Szurman, R. Kocich, J. Drahokoupil, P. Sittner, M. Landa, Evolution of macroscopic elastic moduli of martensitic polycrystalline NiTi and NiTiCu shape memory alloys with pseudoplastic straining, *Acta Mater.* 123 (2017) 146–156.
- [71] R. Hill, A theory of the yielding and plastic flow of anisotropic metals, *Proc. Roy. Soc. Lond. Math. Phys. Sci.* 193 (1948) 281.
- [72] F. Barlat, D.J. Lege, J.C. Brem, A six-component yield function for anisotropic materials, *Int. J. Plast.* 7 (1991) 693–712.
- [73] O. Cazacu, B. Plunkett, F. Barlat, Orthotropic yield criterion for hexagonal closed packed metals, *Int. J. Plast.* 22 (2006) 1171–1194.
- [74] M. Gotoh, A theory of plastic anisotropy based on a yield function of fourth order (plane stress state)—I, *Int. J. Mech. Sci.* 19 (1977) 505–512.
- [75] T. Ezaz, H. Sehitoglu, H.J. Maier, Energetics of (1 1 4) twinning in B2 NiTi under coupled shear and shuffle, *Acta Mater.* 60 (2012) 339–348.
- [76] M. Wj, Mechanical Twinning and Twinless Martensite in Ternary Titanium(50) Nickel(50-x) M(X) Intermetallics, Stanford University, 1991.
- [77] J.M. Ball, R.D. James, F.T. Smith, Proposed experimental tests of a theory of fine microstructure and the two-well problem, *Philos. Trans. R. Soc. London, Ser. A: Physical and Engineering Sciences* 338 (1992) 389.
- [78] R.D. James, Z. Zhang, R.D. James, Z. Zhang, A way to search for multiferroic materials with “unlikely” combinations of physical properties, in: A. Planes, L. Mañosa, A. Saxena (Eds.), *Magnetism and Structure in Functional Materials*, Springer Berlin Heidelberg, Berlin, Heidelberg, 2005, pp. 159–175.
- [79] S.-H. Chang, W.-C. Chiu, Selective leaching and surface properties of Ti50Ni50–xCu_x (x=0–20at.%) shape memory alloys for biomedical applications, *Appl. Surf. Sci.* 324 (2015) 106–113.